Modelling saltation intermittency

Sylvain Dupont, Gilles Bergametti, Beatrice Marticorena, Serge Simo ëns

Modeling saltation intermittency

S. Dupont,[1] G. Bergametti,[2] B. Marticorena,[2] and S. Simoëns[3]

Received 17 January 2013; revised 19 April 2013; accepted 27 May 2013.

[1] In order to investigate the intermittency of the aeolian saltation, a saltation model, forced with instantaneous velocity fields, has been introduced in a Large Eddy Simulation airflow model. The coupled model is evaluated on a flat erodible surface under various wind conditions and soil particle-size distribution. It is first shown that the model is able to simulate a well-developed saltation layer in equilibrium with the turbulent flow. The main characteristics of the saltation layer and their sensitivity to wind conditions are in good agreement with previous data set. Then, the saltation intermittency is visualized through the presence of blowing sand structures near the surface, known as aeolian streamers. This is the first time that such structures are reproduced numerically. From a correlation analysis, we confirm previous thoughts that these sand structures are a visual footprint of past turbulent eddies propagating in the surface boundary layer. The streamers appear to be embedded in larger saltation structures with increasing wind conditions. The spatial scales of these streamers change with wind conditions and soil particle-size distribution. This is explained by two mechanisms: (1) the modification of eddy structures with the main characteristics of the saltation layer, and (2) the reduction of saltating particle sensitivity to the near-surface eddies with increasing wind condition and soil median particle diameter, as the eddy lifetime decreases within the saltation layer and the particle response time increases, respectively. The standard deviation of the saltation flux associated to these saltation patterns represents about 10% to 20% of the mean saltation flux.

Citation: Dupont, S., G. Bergametti, B. Marticorena, and S. Simoëns (2013), Modeling saltation intermittency, *J. Geophys. Res. Atmos.*, *118*, doi:10.1002/jgrd.50528.

1. Introduction

[2] Soil erosion by wind has many environmental, climatic, and health implications. Wind-blown sand is known to modify the topography through the formation of sand dunes and sand ripples [*Bagnold*, 1941; *Shao*, 2008]. But it may also damage young crops or orchard plants through abrasion or immersion/uprooting [*Sterk*, 2003]. Wind-blown dust is responsible (1) at local scales for impoverishing soil in organic matters and nutrients, and so for reducing soil ability to retain moisture [*Field et al.*, 2010], and (2) at large scales for modifying radiative transfers in the atmosphere [*Sokolik et al.*, 2001], impacting cloud and precipitation formation [*Rosenfeld et al.*, 2001; *Yin et al.*, 2002; *Levin et al.*, 2005], and so impacting the energy budget of the Earth [*Miller and Tegen*, 1998; *Tegen*, 2003]. The presence of dust in the atmosphere may induce human health issues related to air quality deterioration [*Bonasoni et al.*, 2004], inhalation of minute particles ($< 10\,\mu$m) [*Derbyshire*, 2007] or spread of disease carried by the particles [*Schlesinger et al.*, 2006; *Bell et al.*, 2008; *Chen et al.*, 2010]. Recent studies also indicated that the deposition of dust on oceans may impact marine biochemistry and climate [e.g., *Schulz et al.*, 2012]. Our concerns on above issues have increased over the last few decades as a consequence of the expansion of drylands over the Earth, resulting from human activities [e.g., *Li et al.*, 2004]. The large range of spatial and temporal scales (from local to global scales) involved in aeolian erosion and the sensitivity of these processes to many factors such as wind conditions, surface heterogeneities (rocks, vegetation cover, and topography), or soil properties (humidity, texture, and mineralogy), show the complexity of the whole soil erosion process. Being able to simulate soil erosion is desired for predicting dust storm or for identifying good landscape management practices to reduce soil erosion. The present study is focusing on modeling wind-blown sand over dry bare soils.

[3] Since the initial work of *Bagnold* [1941], it is well recognized that when the wind becomes sufficiently strong, three modes of aeolian particle motions may appear: creep, saltation, and suspension motions. These modes are related to different ranges of particle diameters composing the erodible surface. Creep motion consists of large particles

Additional supporting information may be found in the online version of this article.

[1]INRA, UR1263 Ephyse, Villenave d'Ornon, France.
[2]LISA (Laboratoire Interuniversitaire des Systèmes Atmosphériques), UMR CNRS 7583 Universités Paris Diderot and Paris Est, Créteil, France.
[3]LMFA, UMR CNRS 5509, Ecole Centrale de Lyon, Université de Lyon I, INSA Lyon, France.

Corresponding author: S. Dupont, INRA, UR1263 Ephyse, 71 Avenue Edouard Bourlaux, FR-33140 Villenave d'Ornon, France. (sylvain.dupont@bordeaux.inra.fr)

2169-897X/13/10.1002/jgrd.50528

(500 to 1000 μm) rolling and sliding along the ground surface without losing contact with the ground due to their large inertia. Smaller particles (20 to 500 μm) lose contact with the ground as forces due to wind shear are able to exceed cohesive forces between soil particles. These particles move through a succession of short bounces along the surface (hopping motion of sand particles). This motion corresponds to the saltation process that remains in the lower first meter of the surface atmospheric boundary layer forming the saltation layer. When reaching the ground, these particles can rebound or splash up other particles, increasing successively the number of particle in saltation. As saltating particles take part of their momentum from the flow, the wind velocity decreases within the saltation layer with the number of saltating particles, until a saltation equilibrium state is reached [*Owen*, 1964]. The saltation bombardment of the ground (sandblasting) can also eject dust particles ($< 20\,\mu$m) that would otherwise remain confined at the surface as their cohesive forces are much larger than for saltating particles. Lifted dust can then be transported away from the saltation layer by turbulent motions and travel over hundreds of kilometers within the atmosphere [*Shao*, 2008] as the gravity force of dust particles is negligible compared to the aerodynamic force. This last motion corresponds to suspension.

[4] Saltation is a key process in soil erosion as it is the primary driver for dust emission. This is why saltation has been largely studied from wind-tunnel [*Shao and Raupach*, 1992; *Nalpanis et al.*, 1993; *Rice et al.*, 1995; *Iversen and Rasmussen*, 1999; *Rasmussen and Sorensen*, 2008] and field experiments [*Greeley et al.*, 1996; *Gillette et al.*, 1997; *Namikas*, 2003]. Research has especially focused on (1) assessing the threshold friction velocity at which saltation is initiated; (2) quantifying the horizontal mass flux of saltating particles following wind intensity, soil particle size, and ground characteristics; (3) assessing the feedback between particles and the flow; and (4) investigating particle-ground interactions (rebound and ejection). From these studies, a large range of saltation models has been developed, going from analytical models [*Sorensen*, 1991; *Raupach*, 1991], semi-empirical parameterization of the threshold friction velocity, the horizontal mass flux, and the saltation roughness length [*Bagnold*, 1937; *Owen*, 1964; *Marticorena and Bergametti*, 1995; *Shao and Lu*, 2000], to complex models accounted for the main physical processes involved in saltation [*Ungar and Haff*, 1987; *Werner*, 1990; *Anderson and Haff*, 1988; *Shao and Li*, 1999; *Andreotti*, 2004; *Almeida et al.*, 2006; *Kok and Renno*, 2009]: particle trajectory resolution, parameterization of the ejection or the splashing of particles from the surface, reduction of the wind speed within the saltation layer, and development to a steady state of the saltation layer. However, most of these complex models are valid for idealized cases and difficulty exportable to heterogeneous environment as the wind is simply represented by a logarithmic profile, although some turbulent fluctuations have been recently added to this profile in the model of *Kok and Renno* [2009]. Only few of these models resolve explicitly the wind flow and its complete interaction with particles, allowing them to be applicable in heterogeneous configuration, although it has never been done. Hence, *Shao and Li* [1999] and *Almeida et al.* [2006, 2007] coupled a saltation model with a Reynolds-averaged type wind-flow model using a statistical $k-\epsilon$ turbulence scheme. However these models only simulated mean wind fields, without simulating explicitly the main turbulent structures present in the surface boundary layer, and they neglected the impact of the turbulence on particle motion.

[5] The process of saltation is very intermittent in time and in space due to the turbulence of the flow and to surface heterogeneities in terms of topography, surface moisture, roughness elements, or soil texture [*Gares et al.*, 1996; *Stout and Zobeck*, 1997; *Jackson et al.*, 2006; *Durn et al.*, 2011]. One visible demonstration of this intermittency is the development of aeolian streamers, known also as sand snakes, over erodible surfaces such as beaches. They correspond to elongated structures with high saltating particle concentration, meandering laterally, merging and bifurcating as they move downwind [*Baas and Sherman*, 2005; *Baas*, 2008]. *Baas and Sherman* [2005] investigated the spatial characteristics and the formation of aeolian streamers from a field experiment. Although they were not able to demonstrate the link between aeolian streamers and the eddies of the flow, they suggested that aeolian streamers are a visual footprint of wind gusts propagating in the surface boundary layer. Hence, the equilibrium state of the saltation layer has only a statistical meaning. Accounting for turbulent structures in saltation models appears therefore important [*Shao*, 2008], especially for quantifying the intermittency of saltation.

[6] The large eddy simulation (LES) technique used in wind flow modeling gives access to instantaneous dynamic fields. With LES, eddy motions larger than twice the grid mesh are explicitly solved whereas subgrid scale eddy motions are modeled. Consequently, LES has the potential of simulating the intermittency of the saltation process when coupled with a saltation model. However, modeling saltation intermittency from a LES approach is still challenging because saltation occurs near the surface, within a layer not exceeding 1 m height, where turbulent eddies are small, modulated by the high concentration of saltating particles, and sensitive to the large-scale eddies of the surface atmospheric layer. Hence, saltation involves a large range of spatial and temporal scales that is still difficult to account for due to computational resource limitation. To our knowledge, the only attempt made so far to couple a LES model with a saltation model has been performed by *Vinkovic et al.* [2006]. Although *Shao and Li* [1999] talked about LES regarding their model, it seems to us that they used a $k-\epsilon$ closure, and so they were not able to simulate explicitly turbulent structures. *Vinkovic et al.* [2006] only validated qualitatively their model on the development of a saltation layer against wind-tunnel measurements, without reaching equilibrium, with a negligible impact of particles on the wind flow, with a monodisperse soil, and they did not investigate the interaction between particle motions and turbulent eddies.

[7] The goals of the present paper are as follows: (1) to present a new model coupling an LES wind flow model with a saltation model based on the previous work of *Vinkovic et al.* [2006], (2) to compare qualitatively and quantitatively the new model against previous observations on a flat erodible soil, for a steady state saltation layer and for various wind conditions and soil particle-size distribution, and (3) to investigate the intermittency of the saltation process in relation to the turbulence structures of the flow.

Table 1. List of Variables

Symbols	Description	Unit
	Latin symbols	
a	constant involved in the calculation of N_{ej}	-
A_N	constant involved in the calculation of u_{*t}	-
A_p	particle section area	m^{-2}
c_p, c_v	specific heat of air at constant pressure and volume	$J\,kg^{-1}K^{-1}$
C_0	Lagrangian constant	-
C_{dp}	particle drag coefficient	-
C_p	vertically integrated number of particles	m^{-2}
C_{pmax}	maximum value of the vertically integrated number of particles	m^{-2}
d_p	particle diameter	m
e	turbulent kinetic energy	$m^2 s^{-2}$
$f(Re_p)$	empirical relation depending on the particle Reynold number Re_p	-
f_y	wave number along the y direction	m^{-1}
F_i	drag force term	$m\,s^{-2}$
g	acceleration due to gravity	$m\,s^{-2}$
G	mean horizontal mass flux	$kg\,m^{-2}s^{-1}$
G_{tot}	total horizontal mass flux	$kg\,m^{-1}s^{-1}$
L_x, L_y, L_z	domain size in x, y and z directions	m
m_j	mass fraction of particles of the jth mode	-
m_p	particle mass	kg
n_j	number of mode	-
n_{pcell}	number of particles in a grid cell	-
N_{ej}	number of newly ejected particles	-
p	air pressure	Pa
prob (v_{ej}), prob (v_{reb})	probability distribution of v_{ej} and v_{reb}	-
P_{reb}	particle rebound probability	-
Q	ratio between the real number of particles and the number of numerically resolved particles	-
R_{cu}	zero time-lag correlation between C_p and u	-
S_c, S_u	average spectra along the y direction of C_p and u	$m^2 s^{-2}$
St	Stoke number	-
t	time	s
T_L	Lagrangian correlation time scale	s
T_p	particle response time scale	s
T_ϵ	lifetime of resolved eddies	s
u, v, w	streamwise, spanwise and vertical wind velocity components	$m\,s^{-1}$
u_*	friction velocity	$m\,s^{-1}$
u_{*t}	threshold friction velocity	$m\,s^{-1}$
u_{*s}	saltation friction velocity	$m\,s^{-1}$
u_i	wind velocity component in direction i	$m\,s^{-1}$
u_{max}	maximum value of the wind velocity	$m\,s^{-1}$
u_{pi}	particle velocity component in direction i	$m\,s^{-1}$
u_{ref}	reference wind velocity at 2 m height	$m\,s^{-1}$
v_{ej}	velocity of newly ejected particle	$m\,s^{-1}$
v_{imp}	impacting velocity of particle	$m\,s^{-1}$
v_{reb}	rebounding velocity of particle	$m\,s^{-1}$
V_{cell}	volume of a grid cell	m^3
x, y, z	streamwise, spanwise and vertical coordinates	m
x_i	coordinate in direction i	m
x_p	particle position	m
z_0	ground roughness length	m
z_{0s}	saltation roughness length	m
z_m	saltation layer height	m
	Greek symbols	
α_{div}	damping coefficient	-
$\alpha_{hej}, \alpha_{hreb}$	particle ejection and rebound angles toward a vertical plane in the streamwise direction of the impacting particle	°
$\alpha_{vej}, \alpha_{vreb}$	particle ejection and rebound angles toward the surface	°
δ_{ij}	Kronecker symbol	-
$\Delta_x, \Delta_y, \Delta_z$	grid resolution in the x, y and z directions	m
ϵ	dissipation rate of the SGS turbulent kinetic energy	$m^2 s^{-3}$
ϵ_{tot}	total dissipation rate of the turbulent kinetic energy	$m^2 s^{-3}$
φ_i	quantity characterizing the wind or the saltating particles in direction i	-
γ	constant involved in the calculation of u_{*t}	$kg\,s^{-2}$
γ_{reb}	empirical parameter	$s\,m^{-1}$
κ	Von Karman constant	-
λ_x, λ_y	mean aeolian streamer length and width	m
μ_j	mass median diameter of the jth mode	m
ν	air molecular kinematic viscosity	$m^2\,s^{-1}$

Table 1. (continued)

Symbols	Description	Unit
$\nu_{\text{th}}, \nu_{tv}$	horizontal and vertical eddy viscosities	m^2s^{-1}
θ	air potential temperature	K
ρ	air density	kg m^{-3}
ρ_p	particle density	kg m^{-3}
σ_G	mean standard deviation of G_{tot}	$\text{kg m}^{-1}\text{s}^{-1}$
σ_j	geometric standard deviation of the jth mode	-
σ_{reb}	standard deviation of the normal distribution of v_{reb}	ms^{-1}
$\sigma_{\alpha\text{hej}}, \sigma_{\alpha\text{vej}}, \sigma_{\alpha\text{hreb}}, \sigma_{\alpha\text{vreb}}$	standard deviation of the normal distribution of α_{hej}, α_{vej}, α_{hreb} and α_{vreb}	°
$\tau_{3\theta}$	subgrid vertical heat flux	K m s^{-1}
τ_{ij}	subgrid stress tensor	m^2s^{-2}
τ_p	particle momentum flux	$\text{kg m}^{-1}\text{s}^{-2}$

2. Model

[8] The Advanced Regional Prediction System (ARPS, version 5.1.5) originally developed at the Center for Analysis and Prediction of Storms (CAPS), University of Oklahoma, is used here for simulating aeolian soil erosion. Initially, ARPS was developed for the explicit prediction of convective and cold-season storms as well as weather systems. A detailed description of the standard version of the model and its validation cases are available in the ARPS User's Manual *Xue et al.* [1995] and in *Xue et al.* [2000, 2001].

[9] For this study, a saltation model has been introduced inside the ARPS model similarly as in *Vinkovic et al.* [2006]. This new model includes (1) a Lagrangian particle motion equation that allows to track individual particle trajectories, (2) a two-way interaction between the turbulent wind flow and particle motions, and (3) a splash scheme to account for particle rebound and ejection at the surface. The saltation layer corresponds to a multiphase flow where particles are assumed spherical with a diameter d_p, a density ρ_p and a mass m_p ($= \pi d_p^3 \rho_p/6$). The atmosphere is considered neutrally stratified, which is a reasonable assumption during saltation events. Finally, the saltation model has been parallelized similarly as the wind flow part of ARPS in order to use the complete model on multiprocessor machines. These modifications introduced in the standard version of ARPS in relation with the saltation model are detailed in the following subsections. Table 1 lists all variables used in this paper.

2.1. Turbulent Wind Flow

[10] ARPS is a three-dimensional, nonhydrostatic, compressible model where Navier-Stokes equations are written in the so-called Gal-Chen or terrain-following coordinates. The grid is orthogonal in the horizontal direction and stretched in the vertical. The model solves the conservation equations for the three wind velocity components, pressure, potential temperature, and water. Wind components and atmospheric state variables (air density, pressure, and potential temperature) are split into a base state (hereafter represented by over-barred variables) and a deviation (double-primed variables). The base state is assumed horizontally homogeneous, time invariant, and hydrostatically balanced. The conservation equations are implicitly filtered toward the grid, in order to separate the small scales from the large scales. Subgrid scale (SGS) turbulent motions, are modeled through a 1.5 order turbulence closure scheme with the resolution of an SGS turbulent kinetic energy (TKE) conservation equation (see Appendix A).

[11] In order to account for the presence of solid particles within the flow, a drag-force term F_i is added in the momentum equation (equation (1)), and its equivalent term is added in the equation for SGS TKE (equation (A1)) in order to preserve the energy budget. As all simulations in this study were performed in a dry, neutrally stratified flow over a flat terrain, the momentum equation presented hereafter is written in Cartesian coordinates for a dry atmosphere. Although the atmosphere is assumed neutral, the potential temperature equation (not shown) has to be solved because turbulent motions are activated through initial turbulent perturbations. The momentum equation, written for a Boussinesq fluid and using the Einstein summation convention, therefore reads

$$\frac{\partial \tilde{u}_i}{\partial t} + \tilde{u}_j \frac{\partial \tilde{u}_i}{\partial x_j} = -\frac{1}{\overline{\rho}} \frac{\partial}{\partial x_i} \left(\tilde{p}'' - \alpha_{\text{div}} \frac{\partial \overline{\rho} \tilde{u}_j}{\partial x_j} \right) - g \left(\frac{\tilde{\theta}''}{\overline{\theta}} - \frac{c_p}{c_v} \frac{\tilde{p}''}{\overline{p}} \right) \delta_{i3} - \frac{\partial \tau_{ij}}{\partial x_j} - F_i, \quad (1)$$

where the overtilde symbol indicates the filtered variables or grid volume-averaged variables, resulting from the grid filtering. In this equation, t is time and x_i ($x_1 = x$, $x_2 = y$, $x_3 = z$) refer to the streamwise, lateral, and vertical directions, respectively; u_i ($u_1 = u$, $u_2 = v$, $u_3 = w$) is the instantaneous velocity component along x_i, δ_{ij} is the Kronecker symbol, α_{div} a damping coefficient meant to attenuate acoustic waves, p the air pressure, ρ the air density, g the acceleration due to gravity, θ the potential temperature; and c_p and c_v are the specific heat of air at constant pressure and volume, respectively. The subgrid stress tensor τ_{ij} is modeled as in *Dupont et al.* [2010] using an eddy viscosity approach where the eddy viscosity is represented as the product of a length scale and a velocity scale characterizing the SGS turbulent eddies. The velocity scale is derived from the SGS TKE (see Appendix A) and the length scale from the grid spacing.

[12] The terms on the right-hand side of equation (1) represent, respectively, the pressure-gradient force term, the buoyancy term, the turbulent transport term, and the drag force term induced by the particles. This latter term is modeled as follows:

$$F_i = \frac{Q}{V_{cell}} \sum_{p=1}^{n_{\text{pcell}}} \frac{1}{2} C_{dp} A_p \left| \vec{\tilde{u}}(x_p) - \vec{u}_p \right| \left(\tilde{u}_i(x_p) - u_{pi} \right), \quad (2)$$

where V_{cell} is the volume of a fluid grid cell, n_{pcell} is the number of numerically resolved particles in the grid cell, $\tilde{u}_i(x_i)$

Table 2. Values of the Saltation Friction Velocity u_{*s}, Threshold Friction Velocity u_{*t} Deduced From *Shao and Lu* [2000], Mass Median Particle Diameter of the Soil μ_1, Ratio Q Between the Real Number of Particles and the Number of Numerically Resolved Particles, Mean Longitudinal λ_x and Lateral λ_y Sizes of Aeolian Streamers, and Mean Lateral Spacing δ_y Between Aeolian Streamers, for the 10 Simulated Cases

Cases	u_{*s} (m s^{-1})	u_{*t} (m s^{-1})	μ_1 (μm)	Q	λ_x (m)	λ_y (m)	δ_y (m)
1	0.41	0.26	200	200	2.7	0.4	0.70
2	0.54	0.26	200	600	2.3	0.3	0.65
3	0.65	0.26	200	1000	1.9	0.4	0.60
4	0.75	0.26	200	1400	2.2	0.4	0.50
5	0.93	0.26	200	3000	1.9	0.3	0.40
6	1.10	0.26	200	4500	0.9	0.3	0.40
7	0.57	0.24	90	28000	0.3	0.2	0.40
8	0.53	0.24	100	15000	0.3	0.2	0.50
9	0.54	0.29	300	200	3.4	0.4	-
10	0.54	0.33	400	50	6.0	2.1	-

is the resolved velocity component of the fluid along x_i at the particle position x_p, u_{pi} ($u_{p1} = u_p$, $u_{p2} = v_p$, $u_{p3} = w_p$) is the instantaneous velocity component of the particle p along x_i, A_p ($= \pi d_p^2/4$) is the section area of the particle p, C_{dp} is the drag coefficient of the particle p (equation (4)), and Q is a constant defined in the next paragraph. Since the resolved fluid velocity components are only available on a discrete grid, their values at the particle position were deduced from a first order trilinear interpolation scheme. In the lower grid cell, the horizontal wind velocity components at the particle position were extrapolated from the resolved fluid components of the second grid cell using a logarithmic profile.

[13] All particle trajectories cannot be explicitly simulated as it would require too much computational resources. Only a statistical representative number of particles is considered in each simulation. In order to simulate the equilibrium state of the saltation process, a ratio Q between the real number of particles and the number of numerically resolved particles is introduced in the expression of F_i (equation (2)). In other words, each resolved particle can be seen as a group of real particles. This approach is similar to the one used in *Almeida et al.* [2006]. In our simulations, Q is constant throughout the domain. Its value is indicated in Table 2 for each simulation. It was verified that the saltation results obtained from our model remain similar with lower values of Q (half values), meaning that the number of particle explicitly simulated is statistically meaningful.

2.2. Particle Motion

[14] As the particle density is much larger than the density of the carrier fluid and the particle diameter much smaller than the Kolmogorov scale, the equation of particle velocity components u_{pi} simplifies as follows [*Wang and Squires*, 1996; *Yamamoto et al.*, 2001; *Vinkovic et al.*, 2006]:

$$m_p \frac{\mathrm{d}u_{pi}}{\mathrm{d}t} = \frac{1}{2}\overline{\rho} C_{dp} A_p \left|\vec{\tilde{u}}(x_p) - \vec{u}_p\right| \left(\tilde{u}_i(x_p) - u_{pi}\right) + m_p g \delta_{i3}, \quad (3)$$

where the terms on the right-hand side of this equation represent the drag and gravity forces. The effect of nonlinear drag is included in an empirical relation of C_{dp} [*Clift et al.*, 1978]:

$$C_{dp} = \frac{24\nu}{\left|\vec{\tilde{u}}(x_p) - \vec{u}_p\right| d_p} f(Re_p), \quad (4)$$

where ν is the molecular kinematic viscosity of the fluid and $f(Re_p)$ is an empirical relation depending on the particle Reynolds number [*Clift et al.*, 1978; *Vinkovic et al.*, 2006].

[15] Although recent studies suggested that interparticle collisions may be significant near the surface for high wind conditions [*Dong et al.*, 2005; *Huang et al.*, 2007], this process has been neglected in this first version of the present model as in most of previous saltation models.

[16] Close to the surface, most turbulent eddies are SGS eddies and are therefore not explicitly simulated by the LES model. Only their effect on large eddies is represented through the SGS turbulence scheme. In order to account for the effects of these SGS eddies on particle motions, *Vinkovic et al.* [2006] developed a SGS stochastic model to compute the SGS particle velocity. In this study, the SGS particle velocity has been neglected as the lifetime of the smallest resolved eddies is smaller than the particle response time (see section 4.2).

[17] For the sake of clarity, the overtilde symbol on $\tilde{u}_i$ will be omitted from now on.

2.3. Particle Interaction With the Surface

[18] The splash scheme introduced inside ARPS derives from the probabilistic models of *Anderson and Haff* [1991], *Shao and Li* [1999], *Andreotti* [2004], *Vinkovic et al.* [2006] and *Kok and Renno* [2009]. It has been adapted for the present LES model, but it keeps the main characteristics of the previous schemes, in particular in term of mean values of rebound-ejection particle velocity, angle, and number. As stated by *Shao* [2008], we should keep in mind that a large part of these previous models relies on hypothetical parameterizations although they have been deduced from either wind-tunnel observations or computational simulations.

[19] The ground or particle bed is composed of particles with various diameters that follow a multimodal mass size distribution as proposed by *Marticorena and Bergametti* [1995] where each mode has a lognormal distribution:

$$\frac{\mathrm{d}M(d_p)}{\mathrm{d}\ln(d_p)} = \sum_{j=1}^{n_j} \frac{m_j}{\sqrt{2\pi}\ln(\sigma_j)} \exp\left(\frac{(\ln d_p - \ln \mu_j)^2}{-2(\ln \sigma_j)^2}\right). \quad (5)$$

In equation (5), n_j is the number of mode, j refers to the jth mode, m_j is the mass fraction of particles of the jth mode, μ_j is the mass median diameter, and σ_j is the geometric standard deviation of the mode lognormal distribution. In simulations

presented hereafter, only one mode of mass size distribution is considered.

[20] Particle aerodynamic entrainment from the surface is neglected as only well-developed saltation conditions are studied here. Therefore, the flow friction velocity is always larger than its saltation threshold value, and only particle rebound and ejection are considered in the model. The breakage of the crystalline structure of mineral particles or of aggregated particles as they impact the surface has been neglected for simplification. When a particle reaches the lower 0.5 mm layer above the surface, the particle is assumed to rebound, eject other particles, or deposit on the surface following its velocity. This layer of 0.5 mm represents a compromise between (1) the difficulty of defining the surface in a well-developed saltation event due to the high concentration of saltating particles at the surface, (2) the neglect of particle rolling along the surface, and (3) the neglect of interparticle collisions that should be important close to the surface.

[21] The probability that a particle rebounds when it impacts the surface is approximated by [*Anderson and Haff*, 1991]:

$$P_{\text{reb}} = 0.95\left(1 - \exp\left(-\gamma_{reb} v_{\text{imp}}\right)\right), \tag{6}$$

where v_{imp} is the impact velocity of the saltating particle and γ_{reb} is an empirical parameter of the order of 2 s m^{-1}.

[22] The rebounding particle is characterized by its velocity (v_{reb}) and angles toward the surface (α_{vreb}) and toward a vertical plane in the streamwise direction of the impacting particle (α_{hreb}). As suggested by *Anderson* [1989], v_{reb} is characterized by a normal distribution:

$$\text{prob}(v_{\text{reb}}) = \frac{1}{\sqrt{2\pi}\sigma_{\text{reb}}} \exp\left(-\frac{(v_{\text{reb}} - \langle v_{\text{reb}}\rangle)^2}{2\sigma_{\text{reb}}^2}\right), \tag{7}$$

where $\langle v_{reb}\rangle = 0.6 v_{\text{imp}}$ is the mean rebound velocity, and $\sigma_{\text{reb}} = 0.25 v_{\text{imp}}$ its standard deviation. The rebound angles follow also a normal distribution with $\langle \alpha_{\text{vreb}}\rangle = 30°$, $\langle \alpha_{hreb}\rangle = 0°$, $\sigma_{\alpha_{\text{vreb}}} = 15°$ and $\sigma_{\alpha_{\text{hreb}}} = 10°$. The angle α_{hreb} is usually not mentioned in previous studies; values used here remain speculative, but they should not impact strongly the saltation process.

[23] The rebounding particle can also eject other particles. The number of newly ejected particles N_{ej} is usually proportional to the impact velocity of the saltating particle. Following *Andreotti* [2004], *Beladjine et al.* [2007] and *Kok and Renno* [2009], N_{ej} is simply modeled as

$$N_{ej} = \frac{a}{\sqrt{g\langle d_p\rangle}} v_{\text{imp}}, \tag{8}$$

where a is a constant that ranges between 0.01 and 0.05 [*Kok and Renno*, 2009] and chosen here equal to 0.03, and $\langle d_p\rangle = \sum_{j=1}^{n_j} m_j \mu_j$ is the mean soil particle diameter.

[24] Similarly as for rebounding particles, newly ejected particles are defined by their initial velocity (v_{ej}), angles toward the surface (α_{vej}), and toward a vertical plane in the streamwise direction of the impacting particle (α_{hej}). *Anderson and Haff* [1988] observed from simulations of single-grain impacts into granular beds that the velocity of the ejected particles v_{ej} increases linearly with v_{imp} for $v_{\text{imp}} < 6$ m s^{-1} and saturates at about 10% of v_{imp} for higher values of v_{imp}. For this reason, *Anderson* [1989] suggested that v_{ej} follows an exponential distribution:

$$\text{prob}(v_{\text{ej}}) = \frac{1}{\langle v_{\text{ej}}\rangle} \exp\left(-\frac{v_{\text{ej}}}{\langle v_{\text{ej}}\rangle}\right), \tag{9}$$

where we chose $\langle v_{\text{ej}}\rangle = 0.08 v_{\text{imp}}$ [*Rice et al.*, 1995]. As for rebounding particles, the ejection angles follow a normal distribution with $\langle \alpha_{\text{vej}}\rangle = 60°$, $\langle \alpha_{\text{hej}}\rangle = 0°$, $\sigma_{\alpha_{\text{vej}}} = 15°$ and $\sigma_{\alpha_{\text{hej}}} = 10°$. The diameters of the newly ejected particles are taken randomly from the multimodal mass size distribution of the soil (equation (5)). This approach is reasonable in the present study as only one dominant population of particle diameters (one mode) is considered in the next simulations. However, for soils with a larger range of particle diameters (several modes), choosing randomly the size of the newly ejected particles could lead to a violation of the conservation of energy or momentum. In that case, our approach should be revised. In the next simulations, it has been verified that, on average, the energy contained in the rebounding and ejecting particles does not exceed the energy of the impacting particle.

2.4. Numerical Details

[25] Ten three-dimensional simulations were performed under a neutral atmosphere on an erodible flat soil characterized by a mass size distribution with only one dominant population (one mode). In the first six simulations (referenced as cases 1 to 6), the mass size distribution of the soil is identical ($\mu_1 = 200\,\mu$m and $\sigma_1 = 1.2$) while the wind condition increases from cases 1 to 6, the saltation friction velocity u_{*s} going from 0.41 to 1.10 m s^{-1}, corresponding to low to very high wind conditions, respectively. In the last four simulations (cases 7 to 10), the wind conditions are similar to that of case 2 (u_{*s} around 0.54 m s^{-1}) but the soil mass median particle diameter changes from $\mu_1 = 90$ to 400 μm with $\sigma_1 = 1.2$. The roughness length z_0 of the soil is identical in all simulations and equal to 10 μm. This value is slightly higher than the roughness length of an homogeneous soil of uniform 200 μm diameter particles (assuming that $z_0 = \mu_1/30$ following *Nikuradse* [1933]), and slightly lower than the roughness length of a homogeneous soil of uniform 400 μm diameter particles. The main differences between these simulations are summarized in Table 2.

[26] As stated in the introduction, modeling saltation intermittency from a LES approach is challenging due to the large range of spatial and temporal scales involves in saltation. On one side, the grid resolution of the model has to be fine enough to simulate reasonably well the main eddies within the saltation layer and to simulate the individual aeolian streamers that should scale around 0.2 m width and few meters long following the field study of *Baas and Sherman* [2005]. On the other side, the computational domain has to be long enough to simulate multiple aeolian streamers and to simulate the large-scale eddies of the atmospheric surface layer. Since our computational resources did not permit to resolve together the main eddies of the saltation layer and the large-scale eddies of the surface atmospheric layer, a compromise has been chosen. All simulations were performed within a unique computational domain, extending over $20 \times 15 \times 12$ m^3. This corresponds to $200 \times 150 \times 100$ grid points in the x, y, and z directions, respectively, and

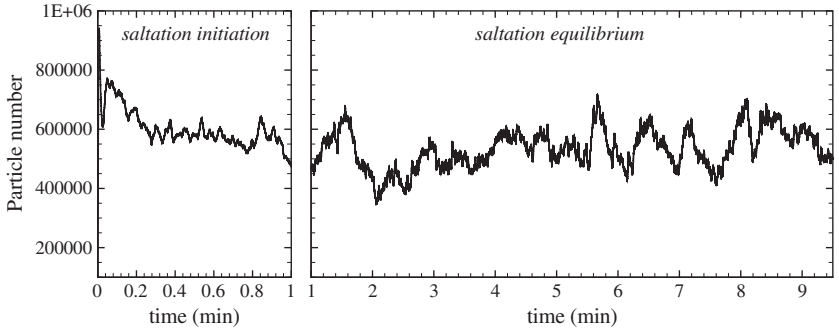

Figure 1. Time variation of the total number of numerically resolved particles within the computational domain of case 2 from the initialization of the saltation to its equilibrium state.

to a horizontal resolution Δx and Δy of 0.10 m. The vertical grid resolution Δz is 0.01 m at the surface, and the grid is stretched above following a cubic function of z, to reach a grid resolution Δz of 0.23 m at the top of the domain. With this resolution, we expect to simulate explicitly aeolian streamers, but the size limitation of the domain does not allow large-scale eddies from the atmospheric surface layer to be resolved since they have a much larger spatial scales than our domain. Finally, the flow and particle motion equations were resolved with the same time step (0.0002 s), which was chosen smaller than the lifetime of the main eddies of the saltation layer and smaller than the response time of particles.

[27] The mean wind is blowing along the x direction. The lateral boundary conditions are periodic for both wind flow and particle motion, which allows to simulate an infinite erodible soil and so a well-developed saltation layer. The bottom wind boundaries are treated as rigid and the surface momentum flux is parameterized by using bulk aerodynamic drag laws. A 3 m deep Rayleigh damping layer is used at the upper boundary in order to absorb upward propagating wave disturbances and to eliminate wave reflection at the top of the domain [*Xue et al.*, 1995]. Additionally, the flow is driven by a depth constant geostrophic wind corresponding to a base state wind at the upper boundary. The velocity fields were initialized using a meteorological preprocessor with a constant vertical profile of potential temperature and a dry atmosphere.

[28] As stated in section 2.1, the number of numerically resolved particles is controlled in the model by the constant Q. In LES simulations of dispersed multiphase flows, the usual approach to determine the number of particles necessary to obtain a representative statistical sample, consists successively (1) in varying the number of particles distributed randomly in the simulated turbulent flow, (2) in calculating the statistics of the flow at the position of the particles, and (3) in comparing them with the flow statistics [*Wang and Squires*, 1996]. A sufficient sample size is reached when both statistics are similar. In presence of saltating particles, this approach cannot be used. Instead, the representative statistical number was deduced from case 2 by verifying that the saltation statistics obtained with this number were identical as the statistics obtained with a double number of particles (Q divided by 2). A similar time-averaged number of particles was then applied in all cases, and we further verified for each case that the time-averaged vertically integrated distribution of particles was continuous in the $x - y$ plane.

[29] Simulations were performed in two steps. The flow dynamic was first solved without saltation. Once the flow dynamic reached an equilibrium state with the soil, then 10 000 initial resolved particles were released randomly within the lower 0.3 m depth layer above the surface, and the saltation model was activated. Saltation events of 10 min were simulated. After the flow and the saltation have reached an equilibrium state, statistics on the wind and saltating particles were computed from a horizontal- and time-averaging procedure. Horizontal averaging was performed over all x and y locations at each considered z, and time averaging was performed over 41 instantaneous three-dimensional samples (including all grid point of the computational domain) collected every 20 s during a 400 s simulation period, starting 200 s after initiating saltation. Consequently, a quantity φ_i characterizing the wind or the saltating particles can be decomposed into $\varphi_i = \langle\varphi_i\rangle + \varphi_i'$, where the symbol $\langle\rangle$ denotes the time and space average and the prime denotes the deviation from the averaged value.

3. Model Evaluation

[30] In this section, the space-time average characteristics of the wind-particle feedback and of the saltation layer obtained from the present model over a bare erodible soil are analyzed and compared against previous results available in the literature.

3.1. Wind Particle Feedback

[31] In order to verify that the simulated saltation layers reach an equilibrium state, Figure 1 shows the time-varying number of resolved particles within the computational domain for case 2, from the release time of saltating particles within the domain ($t = 0$ min) to the simulation end. Just after the release of particles, the number of particles increases drastically due to the splashing process of particles impacting the surface, but rapidly, the number decreases as the wind velocity near the surface is reduced by particles through momentum extraction. This feature corresponds to the saltation overshoot process predicted by *Anderson and Haff* [1991] during the initial stage of development of saltation and before saltation reaches an equilibrium. Latter, *Shao and Raupach* [1992] confirmed from a wind tunnel experiment the presence of this overshoot process

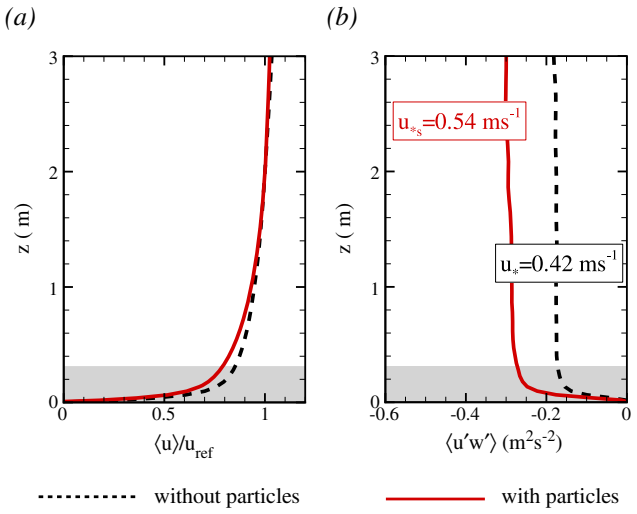

Figure 2. (a) Vertical profiles of the mean horizontal wind velocity $\langle u \rangle$ normalized by its reference value u_{ref} at 2 m height and (b) vertical profiles of the mean momentum flux $\langle u'w' \rangle$, for case 2 with and without saltating particles. The grey area represents the saltation layer.

downwind from the leading edge of a saltating surface. After about $t = 0.5$ min, the number of particles within the computational domain reaches the mean value observed during the next 9 min, meaning that a statistical equilibrium of the particle number within the domain is reached, with a mean value around 600 thousands (which corresponds to $6 \times 10^6 Q$ real particles), and indicating the equilibrium of the saltation layer. The fluctuations of the particle number observed around its mean value confirm that the equilibrium state of the saltation layer has only a statistical meaning. The same behavior of time-varying particle number within the computational domain is observed in all cases.

[32] The behavior of the wind above the erodible surface and its modification due to the presence of saltating particles is now analyzed through the average normalized wind velocity $\langle u \rangle$ and momentum flux $\langle u'w' \rangle$ profiles obtained without and with saltating particles for the case 2 (Figure 2). Other cases give the same profile behavior and are therefore not shown.

[33] Without particles, the flow responds to a constant flux layer where the velocity profile exhibits a logarithmic form and the momentum flux profile is constant. The flow friction velocity u_* is deduced from $\langle u'w' \rangle$ at $z = 2$ m, $u_*^2 = |\langle u'w' \rangle|$, and the roughness length of the soil z_0 is deduced from the logarithmic form of the velocity profile, $\langle u \rangle = (u_*/\kappa) \log(z/z_0)$, where $\kappa = 0.40$ is the Von Karman constant, using a regression procedure. A roughness length of 10 μm is obtained for all simulated cases. The departure of the flow from the characteristics of a constant flux layer is expected near the surface, with a sharper decrease of $\langle u \rangle$ and a decrease of $\langle u'w' \rangle$. Due to the low resolution of the flow near the surface, and to the fact that most of the turbulence near the surface is subgrid scale, this departure starts probably too high in our simulations. However, this discrepancy should not impact significantly saltating particle motions as, very close to the surface, they are not sensitive to the time scales of near-surface turbulent eddies. This point is further discussed in section 4.

[34] With particles, $\langle u \rangle$ exhibits a sharper decrease near the surface than without particles, $\langle u'w' \rangle$ is enhanced throughout all the domain, and the turbulent kinetic energy is reduced near the surface (figure not shown). These flow modifications are explained by the extraction of momentum from the flow by particles through drag force, added with an enhancement of the turbulence dissipation and of the apparent roughness length of the surface (see further). Still a logarithmic profile and a constant momentum flux are observed above about $z = 0.30$ m but with different values of the friction velocity and roughness length compared to the case without particles, corresponding to the saltation friction velocity u_{*s} and to the saltation roughness length z_{0s}, respectively. This behavior is consistent with the simulations of *Shao and Li* [1999]. The friction velocities u_{*s}

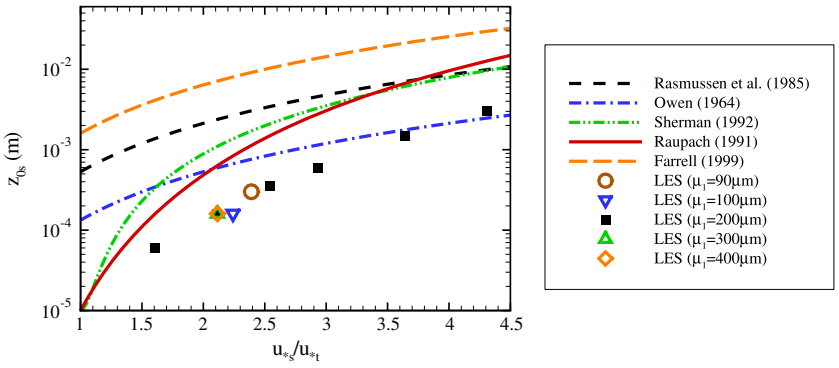

Figure 3. Comparison between simulated (dots) and semiempirical (lines) saltation roughness length z_{0s} against the saltation friction velocity u_{*s} normalized by the threshold friction velocity u_{*t}. The semiempirical z_{0s} are deduced from current expressions available in the literature as summarized in *Sherman and Farrell* [2008] and *Shao* [2008]: (1) $z_{0s} = C_c u_{*s}^2/g$ with $c_c = 0.08$ [*Rasmussen et al.*, 1985], $c_c = 0.24$ [*Farrell*, 1999], $c_c = 0.02$ [*Owen*, 1964]; (2) $z_{0s} = \left(A u_{*s}^2/2g\right)^{1-r} z_0^r$ with $r = u_{*t}/u_{*s}$ and $A = b_r \alpha^2 \exp(-\eta/G_r)$, $b_r = 8$, $\alpha = 0.63$, $\eta = 0.577216$ and $G_r = 1$ [*Raupach*, 1991; *Shao*, 2008], and (3) $z_{0s} = C_m (u_{*s} - u_{*t})^2/g + z_0$ with $C_m = 0.132$ [*Sherman*, 1992]. The threshold friction velocity u_{*t} was deduced from the empirical expression of *Shao and Lu* [2000].

obtained above the saltation layer are given in Table 2 for all simulated cases.

[35] The values of z_{0s} obtained from the present model as a function of u_{*s} normalized by its threshold value u_{*t} are presented in Figure 3. Here u_{*t} was deduced from the parameterization proposed by *Shao and Lu* [2000]: $u_{*t}^2 = A_N\left(\left(\rho_p - \overline{\rho}\right) g\langle d_p\rangle/\overline{\rho} + \gamma/\left(\overline{\rho}\langle d_p\rangle\right)\right)$ with $A_N = 0.0123$ and $\gamma = 3 \times 10^{-4}\,\mathrm{kg\,s^{-2}}$, which was preferred than the *Bagnold*'s [1941] one, since it accounts for particle cohesive force and aerodynamic lift. On the same figure, the values of z_{0s} obtained from the *Charnock* [1955], modified Charnock [*Sherman and Farrell*, 2008], and *Raupach* [1991] relationships applied for field conditions are presented for comparison. Note that recent analytical models of z_{0s} based on physical principles [*Durn and Herrmann*, 2006; *Pahtz et al.*, 2012] are not presented here due to their complexity. The saltation roughness lengths of the different parameterizations exhibit a large variability in magnitude. The values of z_{0s} obtained from the present model appear to increase with u_{*s}, independently on soil particle-size distribution (cases 7 to 10). This trend is in agreement with previous observations, with a closer match with the one predicted by *Raupach*'s [1991] parameterization. However, z_{0s} appears lower than *Raupach*'s [1991] prediction with a difference going up to an order of magnitude for high wind conditions. The reviews of *Shao* [2008] and *Sherman and Farrell* [2008] on the various existing parameterization of z_{0s} showed that z_{0s} is smaller by about an order of magnitude in wind tunnel condition than in field condition for similar wind conditions. Hence, the values of z_{0s} obtained from our model are closer to wind tunnel conditions than field conditions. The reason for this difference between wind tunnel and natural environment is still not well understood [*Shao*, 2008]. *Raupach* [1991] argued that it could be related to the equilibrium of the saltation layer that is usually not fully reached in wind tunnel experiment. More recently, *Sherman and Farrell* [2008] suggested that the inability of wind tunnel experiment to reproduce the large coherent structures of the atmospheric boundary layer could explain the discrepancy between wind tunnel and field experiments. Similarly as wind tunnel conditions, our simulations do not account for the largest coherent structures of the surface atmospheric layer because of the limited size of our computational domain (see section 2.4). This could explain the lower values of z_{0s} obtained from our model compared to field condition but other explanations could be advanced such as the idealized particle bed used in our simulation compared to complex heterogeneous sand beds in natural conditions.

[36] In conclusion, the saltation process reaches an equilibrium with the wind flow. The mean characteristics of the simulated wind flow in presence of saltating particles are consistent with previous observations. These results give us confidence in the ability of the present model to simulate accurately the mean interaction between the wind flow and the saltation layer.

3.2. Saltation Layer

[37] There is no consensus on the definition of the height z_m of the saltation layer as it is usually difficult to determine it from measurements. It is usually assessed as the height below which a certain percentage of the total mass flux is reached. Only few studies reported values of z_m with contradictory behaviors of z_m with wind conditions [*Dong et al.*, 2012; *Kok and Renno*, 2008]. We found it more appropriate here to define z_m as the height above which particles have a negligible impact on the mean wind flow. Hence, z_m was deduced as the height where the particle momentum flux $\tau_p(z)$ reaches 0.1% of the above flow momentum flux ρu_{*s}^2, which corresponds approximatively to the height below in which 99.5% of the total mass flux is present. Here τ_p was computed as

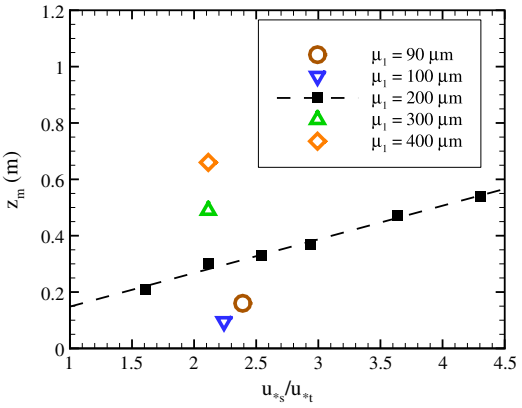

Figure 4. Saltation height z_m as a function of the saltation friction velocity u_{*s} normalized by the threshold friction velocity u_{*t}, deduced from the 10 simulated cases.

$$\tau_p(z) = \left\langle \frac{Q}{L_x L_y \Delta z} \sum_p m_p u_p' w_p' \right\rangle, \tag{10}$$

where the sum is performed on numerically resolved particles located between z and $z + \Delta z$; L_x and L_y are the length and width of the computational domain, 20 and 15 m, respectively.

[38] Figure 4 presents, for all cases, z_m as a function of u_{*s}/u_{*t}. For the same soil particle-size distribution ($\mu_1 = 200\,\mu\mathrm{m}$), z_m increases linearly with u_{*s}, from 0.22 m to 0.55 m, for $u_{*s} = 0.41$ to $1.10\,\mathrm{ms^{-1}}$, respectively. Note that the same tendency has been observed when z_m is deduced from the horizontal mass flux profile instead of the particle momentum flux profile. This behavior of z_m with u_{*s} is consistent with the classic saltation theory of *Bagnold* [1941] and *Owen* [1964], although they predicted an increase of z_m in u_{*s}^2, and consistent with the wind tunnel and field measurements of *Dong et al.* [2006] and *Dong et al.* [2012], respectively, and with the model prediction of *Kok and Renno* [2009]. On the other hand, it is in contradiction with *Kok and Renno* [2008] who extracted z_m from the field experiments of *Greeley et al.* [1996] and *Namikas* [2003] and found no clear tendency of z_m with wind conditions. *Kok and Renno* [2008] argued that the constant value of z_m with wind conditions could be related to the role of sand electrification in saltation, but this explanation needs further research.

[39] Under similar wind conditions (similar u_{*s}), z_m reaches a minimum value for a median soil particle diameter of $\mu_1 = 100\,\mu\mathrm{m}$. This feature is explained by the balance between inertia, gravity, and drag forces applying on airborne particles. Hence, for $100 < \mu_1 < 400\,\mu\mathrm{m}$, the largest

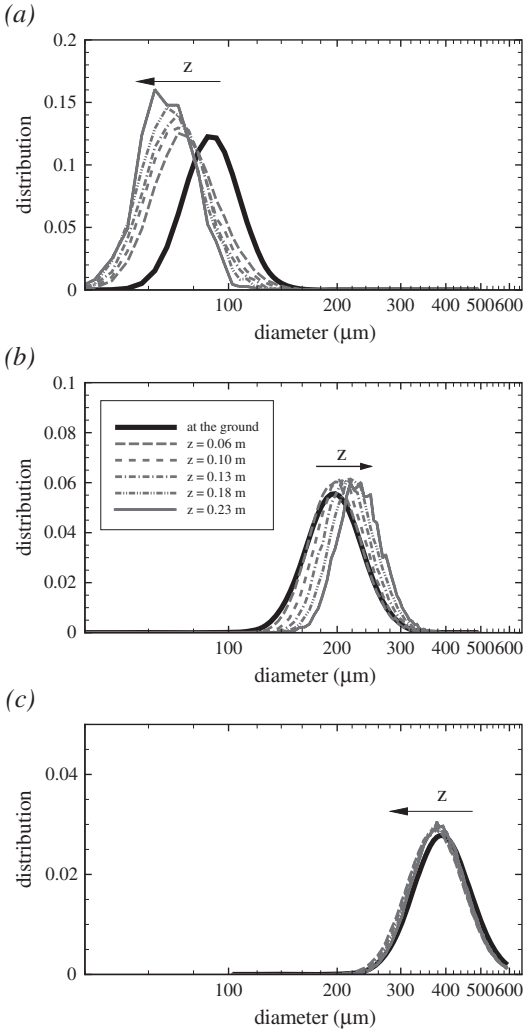

Figure 5. Particle-size distribution within the saltation layer compared to the distribution at the ground, for (a) $\mu_1 = 90\,\mu m$, (b) $\mu_1 = 200\,\mu m$, and (c) $\mu_1 = 400\,\mu m$.

particles impact the ground with higher velocities due to their larger gravity, and so rebound or eject particles that go higher. For $\mu_1 > 400\,\mu m$, we suspect that the gravity force becomes much larger than the drag and inertia forces, decreasing the height of particle trajectories and so the saltation height. On the other hand, for $\mu_1 < 100\,\mu m$, the gravity force becomes much lower than the drag force, and so, particles start to be transported higher by turbulence structures of the flow, reaching the limit between saltation and suspension motions. This sensitivity of the height of particle loops to particle size has been also shown by *Shao and Li* [1999], and is confirmed here by the distribution of particle sizes with height compared to that on the ground (Figure 5). For $\mu_1 = 200\,\mu m$ (Figure 5b), as well as $\mu_1 = 300\,\mu m$ (not shown), larger particles are observed in the upper saltation layer than at the surface; for $\mu_1 = 400\,\mu m$ (Figure 5c), the distribution is almost constant with height, going slightly toward smaller particles with height; and for $\mu_1 = 90\,\mu m$ (Figure 5a) and $\mu_1 = 100\,\mu m$ (not shown), smaller particles are observed in the upper saltation layer with increasing height. *Gillette and Chen* [1999] analyzed also the size distribution of airborne particles within the saltation layer. However, their results are difficult to compare with the present ones since field measurements include also suspension particles, these latter ones resulting from sandblasting of the surface by saltating particles.

[40] Within the saltation layer, the decrease of the wind velocity is accentuated as a transfer of momentum from the flow to saltating particles occurs. The mean particle momentum flux profiles τ_p are presented for cases 1 to 6 in Figure 6a, corresponding to various wind conditions, and for cases 2 and 7 to 10 in Figure 6b, corresponding to various soil particle-size distributions. The particle momentum flux τ_p increases exponentially with depth as expected from *Owen*'s [1964] saltation model and observed by *Shao and Li* [1999] with their numerical model. At the surface, τ_p increases with u_{*s}, to reach about 50% of the above flow momentum flux in case 6. For similar wind conditions, $\tau_p / \left(\rho u_{*s}^2\right)$ exhibits a similar shape for soils with $\mu_1 \geq 200\,\mu m$, while for soils with $\mu_1 \leq 100\,\mu m$, the flow momentum near the surface is almost totally absorbed by particles.

[41] The vertical profiles of the mean horizontal mass flux $\langle G \rangle$ normalized by the total flux $\langle G_{\text{tot}} \rangle$ are presented for cases 1 to 6 in Figure 7a, and for cases 2 and 7 to 10 in Figure 7b. The instantaneous horizontal mass flux was computed as follows:

$$G(x,y,z) = \frac{Q}{\Delta x \Delta y \Delta z} \sum_p m_p u_p, \tag{11}$$

where the sum is performed on numerically resolved particles located between x and $x + \Delta x$, y, and $y + \Delta y$, and z and $z + \Delta z$. As observed in previous wind tunnel experiments [*Nalpanis et al.*, 1993; *Greeley et al.*, 1996; *Rasmussen and Sorensen*, 2008], $\langle G \rangle$ decreases exponentially with height, the slope increasing with u_{*s}. For similar wind conditions, the normalized profiles of $\langle G \rangle$ are identical for soils with $\mu_1 \geq 200\,\mu m$, except near the surface where $\langle G \rangle / \langle G_{\text{tot}} \rangle$ decreases with increasing μ_1. On the other hand, for $\mu_1 \leq 100\,\mu m$, the decay of $\langle G \rangle$ is more than exponential, which explains the complete extraction of the flow momentum by particles observed near the surface in Figure 6b.

[42] The total saltation flux $\langle G_{\text{tot}} \rangle$ is the main output in saltation studies as it quantifies the intensity of the soil erosion. Figure 8 presents $\langle G_{\text{tot}} \rangle$ simulated by the present model as a function of u_{*s}/u_{*t}. For comparison, values obtained from various parameterizations with saltating particles of $200\,\mu m$ diameter are presented on the same figure. As for z_{0s}, *Durn and Herrmann* [2006], *Pahtz et al.* [2012] and *Lammel et al.* [2012] proposed physically based parameterizations that are not presented here due to their complexity. The saltation flux simulated by the present model increases exponentially with u_{*s}, as previously observed. The magnitude of $\langle G_{tot} \rangle$ is consistent with the various parameterizations. For low friction velocities, $\langle G_{\text{tot}} \rangle$ is closer to the parameterization of *Bagnold* [1937] and for high friction velocities, closer to the parameterization of *Sorensen* [2004]. While the values of $\langle G_{\text{tot}} \rangle$ appear similar for soils with $\mu_1 \geq 200\,\mu m$, they increase for soils with μ_1 lower than $100\,\mu m$. This last feature means that a larger mass of saltating particles is required to reach a saltation layer in equilibrium with the flow for soils with small particle diameters. This larger mass of

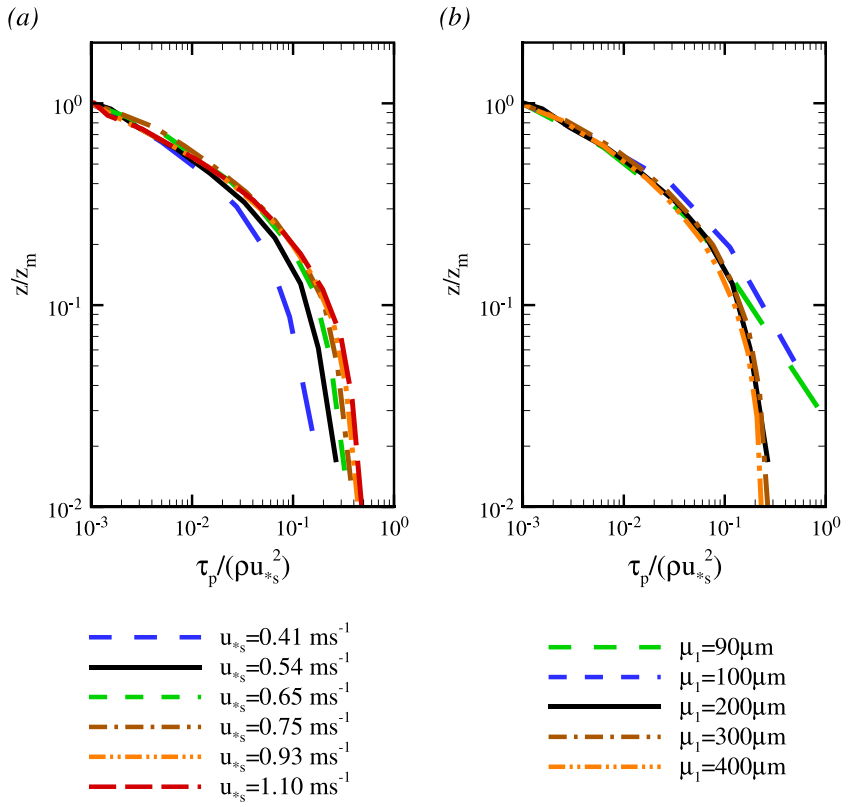

Figure 6. Vertical profiles of the mean particle momentum flux τ_p normalized by the flow momentum flux ρu_{*s}^2 above the saltation layer, for cases with (a) various saltation friction velocities u_{*s} and (b) various soil median particle diameters μ_1.

particle is mainly concentrated near the surface as shown by the profiles of the saltation flux.

[43] In conclusion, the model is able to simulate qualitatively and quantitatively the main characteristics of saltation processes of an erodible flat surface. We observed that for soils with small particle sizes ($\mu_1 \leq 100\,\mu$m) some characteristics of the saltation layer differ from the usual behavior, related to a superior concentration of particles near the surface. For these small particles, saltation and suspension motions may coexist, and the spatial resolution of our computational domain may not be sufficient close to the surface (see section 4.4).

4. Particle-Eddy Interaction

[44] The novelty of our model compared to previous ones is to simulate explicitly turbulent eddies of the flow and their complete interaction with saltating processes. In this section, we analyze the instantaneous behavior of the saltation processes simulated by our model, with a particular focus on aeolian streamers and their consequences on the saltation flux variability.

4.1. Visualization of Aeolian Streamers

[45] Aeolian streamers are defined as elongated patterns of high concentration of wind-blown sand in the streamwise direction. In order to detect the presence of such patterns in our simulations, Figure 9a presents an instantaneous view of the vertically integrated particle concentration C_p field, normalized by its maximum value C_{pmax}, in the horizontal section $x - y$ for case 1. We can see that the concentration field is spatially heterogeneous with the presence of elongated patterns in the direction of the flow, corresponding to high sand concentration regions surrounded by regions with low concentration, similar as individual aeolian streamers. An animation of this sand concentration field shows that these elongated structures meander, merge, or bifurcate over time, similarly as aeolian streamers observed by *Baas and Sherman* [2005] (see the animation presented in the supporting information).

[46] The length λ_x and width λ_y of these streamers were estimated from time-average spatial autocorrelation of C_p in the horizontal section. We defined the core of the streamer as the region where the autocorrelation is higher than 0.4. This value allows to extract the core of the streamers without accounting for the low background correlation remaining in some cases (mostly cases with large particle diameters) over a long distance in the streamwise direction. For case 1, streamers are about 2.7 m long, 0.4 m width (Table 2). The two-dimensional Fourier transform of C_p averaged in time and over longitudinal wavelengths shows a well-defined maximum around 0.7 m for case 1 (Figure 10), corresponding to the mean lateral spacing δ_y between streamers. These values of λ_y and δ_y are of the same order as the 0.2 m width and 1.0 m lateral spacing reported by *Baas and Sherman* [2005]. The mean streamer length was not explicitly reported by *Baas and Sherman* [2005]. However, (A. Baas, personal communication, 2013) indicated that he observed a lifetime of streamers of the order of 0.5 to 1.0 s

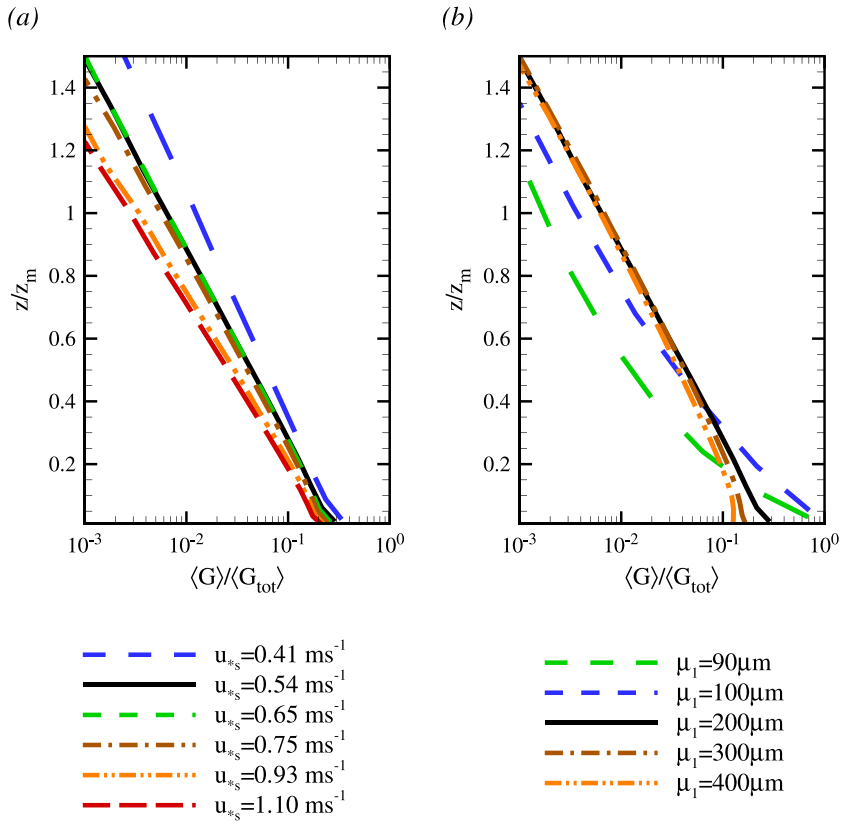

Figure 7. Same as Figure 6 but for the mean saltation flux $\langle G \rangle$ normalized by the total saltation flux $\langle G_{tot} \rangle$.

and a propagation speed of 3.6 m s^{-1} [*Baas and Sherman*, 2005]. This yields to streamer lengths of about 1.8 to 3.6 m, which compares very favorably with the range of λ_x values obtained from the present model. With increasing friction velocity u_{*s} and decreasing soil median particle diameter μ_1 (Table 2), we observed that δ_y decreases. The well-defined spectral peak observed in case 1 becomes a slight bump for high wind conditions or even nonexistent for large soil particle diameters (Figure 10). This may indicate that streamers become less visible with increasing wind conditions or with increasing soil particle diameters. Similarly, λ_x decreases with increasing u_{*s} and decreasing μ_1, while λ_y remains

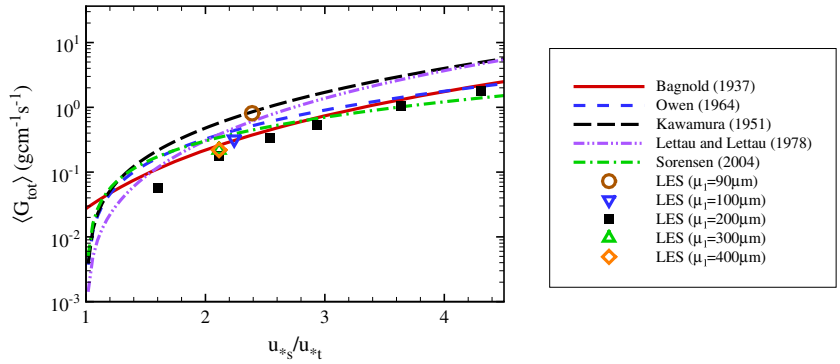

Figure 8. Comparison between simulated (dots) and semiempirical (lines) total saltation flux $\langle G_{\rm tot} \rangle$ against the flow friction velocity u_{*s} normalized by the threshold friction velocity u_{*t}. The semiempirical $\langle G_{\rm tot} \rangle$ is deduced from current expressions available in the literature as summarized in *Shao* [2008] and *Kok and Renno* [2009]: (1) $\langle G_{\rm tot} \rangle = c\sqrt{\langle d_p \rangle / D}\rho u_{*s}^3/g$ with $D = 250\,\mu$m and $c = 1.5$ [*Bagnold*, 1937]; (2) $\langle G_{\rm tot} \rangle = c\rho u_{*s}^3 \left(1 - u_{*t}^2/u_{*s}^2\right)/g$, with $c = 0.25 - \omega_t/3u_{*s}$ where $\omega_t = -1.66\sqrt{\rho_p g \langle d_p \rangle}$ is the particle terminal velocity [*Owen*, 1964]; (3) $\langle G_{\rm tot} \rangle = c\rho u_{*s}^3 \left(1 + u_{*t}/u_{*s}\right)\left(1 - u_{*t}^2/u_{*s}^2\right)/g$ with $c = 2.61$ [*Kawamura*, 1951; *White*, 1979]; (4) $\langle G_{\rm tot} \rangle = c\sqrt{\langle d_p \rangle / D}\rho u_{*s}^3 \left(1 - u_{*t}/u_{*s}\right)/g$ with $D = 250\,\mu$m and $c = 4.2$ [*Lettau and Lettau*, 1978]; (5) $\langle G_{\rm tot} \rangle = \rho u_{*s}^3 \left(1 - u_{*t}^2/u_{*s}^2\right)\left(\alpha + \gamma u_{*t}/u_{*s} + \beta u_{*t}^2/u_{*s}^2\right)/g$ with $\alpha = 0$, $\gamma = 3.0$ and $\beta = 3.9$ [*Sorensen*, 2004]. The threshold friction velocity u_{*t} was deduced from the empirical expression of *Shao and Lu* [2000].

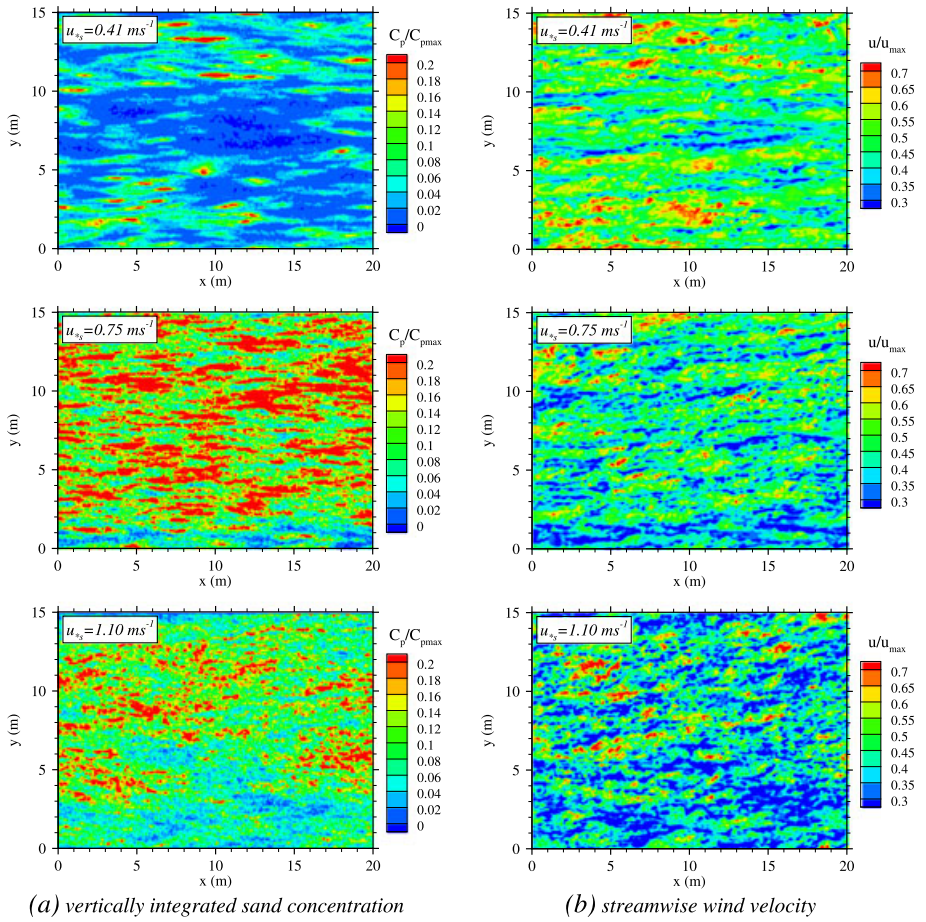

Figure 9. Snapshot of horizontal cross sections ($x - y$) of (a) the vertically integrated sand concentration C_p normalized by its maximum value C_{pmax}, and (b) the streamwise wind velocity u at $z = 0.1$ m normalized by its maximum value u_{max}, for cases 1, 4, and 6 (from the top to the bottom).

constant with u_{*s} and increases with μ_1. For the largest u_{*s} (1.10 m s^{-1}) and the smallest μ_1 (90 and 100 μm), the spatial sizes of the streamers become close to the spatial resolution of the wind flow. The independence of λ_y with the mean airflow characteristics was also observed by *Baas and Sherman* [2005]. On the other hand, they did not observe any sensitivity of δ_y with wind conditions conversely to the present results.

[47] Three different saltation transport patterns were identified by *Baas and Sherman* [2005] following wind conditions: (1) "streamer families" for low wind condition, where individual elongated regions of pronounced saltation are observed surrounded by regions of low or no transport, (2) "nested streamers" for medium wind condition, where multiple elongated regions of high saltation superpose on large scale elongated regions of lower saltation, and (3) "embedded streamers" for high wind condition, where elongated regions of very high saltation are embedded in a large scale saltation cloud. This evolution of the saltation transport pattern from individual to embedded streamers with increasing wind conditions is clearly visible from our simulations (Figure 9a). In low wind conditions ($u_{*s} \leq 0.55$ m s^{-1}), we observed multiple individual streamers surrounded by very low saltation regions, even regions without saltation (concentration lower than 10 real particles per meter square), corresponding to the first two transport patterns. In intermediate wind conditions ($0.55 \leq u_{*s} \leq 0.65$ m s^{-1}), smaller elongated structures of very high sand concentration are present within large scale structures, itself embedded in a background saltation, corresponding to the "embedded streamers" pattern. In high wind conditions ($u_{*s} \geq 1.10$ ms^{-1}), we do not see anymore streamers but large-scale patterns of very high saltation. These saltation transport patterns are also modified with the soil particle-size distribution (figure not shown). Hence, for small particle diameter ($\mu_1 = 90$ μm), we do not see elongated structures but mostly small patches of high saltation concentration, while for large particle diameter ($\mu_1 = 400$ μm), streamers appear longer and larger embedded in large-scale structures that scale with the computational domain size.

[48] In conclusion, aeolian streamers are present in most of our simulations. Their spatial sizes appear to depend on the wind condition and on the soil particle-size distribution. The variations of the saltation transport patterns simulated by the present model following the wind condition are in good agreement with the three transport patterns identified by *Baas and Sherman* [2005]. In order to understand the sensitivity of the streamer size and of the saltation transport

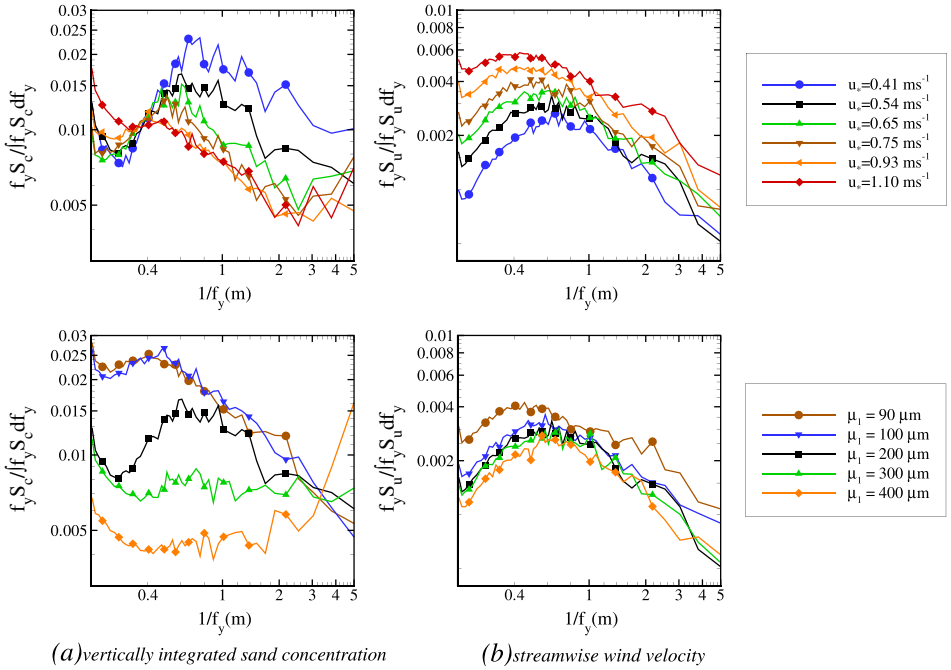

Figure 10. Average spectra along the spanwise direction (a) of the vertically integrated sand concentration C_p and (b) of the resolved-scaled streamwise wind velocity at $z = 0.1$ m, for (top) cases with various saltation friction velocities u_{*s} and (bottom) various soil median particle diameters μ_1.

pattern to the wind condition and to the soil particle-size distribution, the relationship between streamers and turbulent eddies has to be clarified.

4.2. Aeolian Streamers and Turbulent Eddies

[49] Figure 9b presents instantaneous streamwise wind velocity fields u at 0.1 m height, normalized by its maximum value $u_{\max}$, for the simulated cases 1, 4, and 6, corresponding to the same instant as the sand concentration fields C_p presented in Figure 9a. In cases 1 and 4, similar elongated patterns are present in u and C_p fields. The presence of elongated patterns in u fields is well known in neutrally stratified flow. These structures have been observed at small scales in near-wall engineering studies [*Pope*, 2000; *Bhaganagar et al.*, 2004] as well as at larger scales in the surface atmospheric boundary layer [*Drobinski and Foster*, 2003]. In both cases, these structures are known as streaky structures or streaks. The origin and link between streaky structures of different scales is still an ongoing research issue. It is however believed that large scale streaky structures are composed of hairpin or horseshoe vortex packets [*Adrian et al.*, 2000; *Hommema and Adrian*, 2003]. Furthermore, streaky structures may result from the surface blocking of the vertical velocity component of impinging eddies [*Drobinski and Foster*, 2003; *Fesquet et al.*, 2009], and their size characteristics may depend on the roughness of the surface and on the boundary layer depth [*Drobinski and Foster*, 2003; *Bhaganagar et al.*, 2004]. Hence, the smaller size of the flow streaky structures observed with increasing wind condition could be explained by the increase of the saltation roughness length observed in section 3.1. The high sand concentration patterns (Figures 9a) correlate mostly with the high wind speed patterns (Figures 9b). The two-dimensional Fourier transforms of u at 0.1 m height averaged in time and over longitudinal wavelengths exhibit well-defined peaks corresponding to the mean lateral spacing between streaks (Figure 10b). The positions of these peaks correlate very well with those from the sand concentration fields when peaks exist (Figure 10a). On the other hand, in case 6 (highest wind condition), the correlation between the sand concentration and the wind velocity fields is hardly visible (Figure 9), although streaky structures are present in the wind velocity field.

[50] In order to better characterize the correlation between C_p and u, the mean vertical profiles of the zero time-lag correlation between both quantities have been computed following equation (12) for all simulated cases and are presented in Figure 11a for cases 1 to 6 and in Figure 11b for cases 2 and 7 to 10.

$$R_{cu}(z) = \frac{\left\langle C_p'(x,y)u'(x,y,z)\right\rangle}{\sqrt{\left\langle C_p'(x,y)^2\right\rangle}\sqrt{\langle u'(x,y,z)^2\rangle}} \tag{12}$$

[51] Close to the surface, C_p and u appear anti-correlated in all cases (negative values of R_{cu}), high concentration being correlated with low wind velocity. Although u should be taken with caution in the first grid cell, we explain this feature by the momentum extraction from the flow by particles in high sand concentration regions. In simulations where individual aeolian streamers were clearly visible (cases 1 to 4), the correlation reaches a significant maximum between 0.1 and $0.2z_m$ height. The magnitude of this maximum as well as its height decrease with u_{*s}. In the upper saltation layer ($z \geq 0.6z_m$), the correlation reaches a constant value of 0.3 for all cases with $\mu_1 = 200\,\mu$m, independently on u_{*s}. This indicates that sand concentration is also correlated with large-scale eddies. Note that time-lag correlations between sand concentration and past streamwise wind veloc-

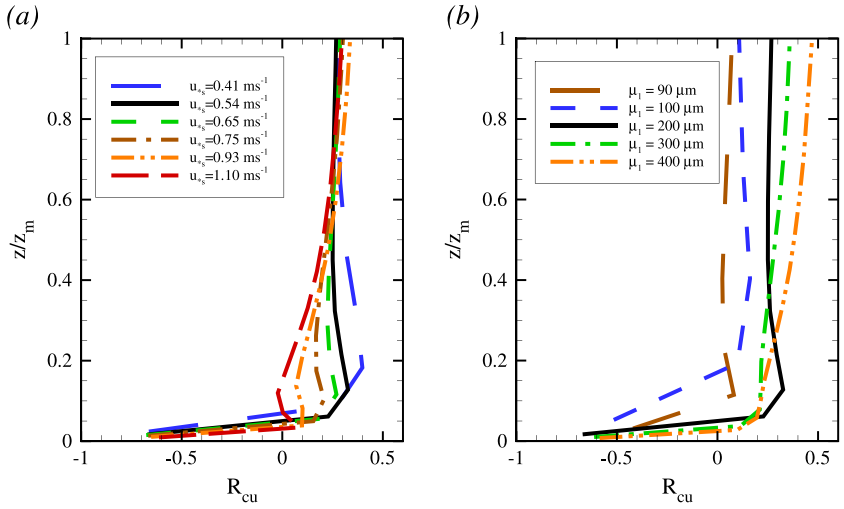

Figure 11. Mean vertical profiles of the zero time-lag correlation R_{cu} between the vertically integrated sand concentration C_p and the streamwise wind velocity $u(z)$, for cases with various saltation friction velocities u_{*s} (a) and various soil median particle diameters μ_1 (b).

ity may show larger correlation magnitude in the upper saltation layer than the zero time-lag correlations presented here. Hence, in high wind conditions, the saltation patterns correlate mostly with large-scale eddies from the upper saltation layer while for low wind conditions they correlate with both near-surface and large-scale eddies, which is consistent with the embedded pictures of *Baas and Sherman* [2005]. With increasing soil median particle diameter, R_{cu} increases in the upper saltation layer, to reach values even larger than that of case 2 with $\mu_1 = 200\,\mu\mathrm{m}$. This feature means that saltation patterns over soils with large particle diameters are more sensitive to large-scale eddies and less to close-surface eddies. For soil with small particles ($\mu_1 \leq 100\,\mu\mathrm{m}$), the correlation is near zero throughout the saltation layer. The correlation with close-surface eddies is maximum for the soil with $\mu_1 = 200\,\mu\mathrm{m}$.

[52] In order to understand the reason for the sensitivity of the saltation patterns to different eddy sizes following u_{*s} and μ_1, the particle response time-scale ($T_p = \rho_p \langle d_p \rangle^2 / (18\overline{\rho}\nu)$) needs to be compared with the lifetime of the resolved eddies (T_ϵ), the ratio between both time scales defining the Stokes number, $St = T_p/T_\epsilon$. In regions where $St << 1$, the particles should follow strictly the flow, while in region where $St >> 1$, the flow should have a negligible effect on particle trajectories. Here, T_ϵ is deduced from the ratio between TKE and its dissipation rate ϵ_{tot}, $T_\epsilon = 0.5 \left\langle u_i'^2 \right\rangle / \epsilon_{\mathrm{tot}}$ [*Kaimal and Finnigan*, 1994]. The variable ϵ_{tot} is deduced from the TKE dissipation rate terms of the budget equation of the mean resolved-scale wind velocity variance, itself deduced following the procedure described in *Stull* [1988], assuming neutral stratification, steady state flow, and homogeneity in the horizontal directions. Here, ϵ_{tot} includes the dissipation of TKE by particle drag and the transfer of TKE between resolved and SGS motions:

$$\epsilon_{\mathrm{tot}} = \left(\left\langle u_i' u_i' \right\rangle - \left\langle u_i' u_{pi}' \right\rangle \right) \left\langle \frac{Q}{V_{\mathrm{cell}}} \sum_{p=1}^{n_{\mathrm{pcell}}} \frac{m_p}{\overline{\rho}} \frac{f(R_{\mathrm{ep}})}{T_p} \right\rangle - \left\langle \tau_{ij}' \frac{\partial u_i'}{\partial x_j} \right\rangle. \quad (13)$$

[53] Figures 12a and 12b present the profiles of St obtained within the saltation layer following u_{*s} (cases 1 to 6) and μ_1 (cases 2 and 7 to 10), respectively. In all cases, St appears much higher than 1 near the surface, meaning that particles are not sensitive to local turbulent eddies. This confirms that SGS eddies have a negligible impact on particle motions. Then, St decreases rapidly with height, reaching values lower than 1 above about $0.1 z_m$ for cases with $\mu_1 \geq 200\,\mu\mathrm{m}$, above 0.3–$0.4 z_m$ for other cases. In these last cases, the discontinuous profiles of St near the surface is probably due to the low resolution of the saltation layer. The decrease of St with z/z_m is slower with increasing u_{*s} while it is similar for $\mu_1 \geq 200\,\mu\mathrm{m}$. In other words, particles near the surface, i.e., most of the saltating particles, are increasingly influenced by near-surface eddies with decreasing wind conditions. This last process is accentuated by the fact that the saltation layer height increases with u_{*s}. This feature explains (1) that streamers are more visible in low wind conditions (section 4.2) and (2) that correlation profiles between C_p and u exhibit a maximum around 0.1 and $0.2 z_m$ for low wind conditions and above $0.6 z_m$ for high wind conditions. The slower vertical decrease of St with increasing u_{*s} is explained by the decrease of the eddy lifetime as the eddy convection velocity increases and the rate of eddy dissipation is enhanced with the saltation flux. With increasing particle diameter, particles become less sensitive to near-surface eddies as their response time-scales increase. Hence, streamers are less visible and embedded in a higher saltation background. On the other hand, sand concentration fields correlate more with higher wind field as the saltation height increases, involving eddies with longer lifetime in the saltation process.

[54] In conclusion, aeolian streamers appear clearly related to elongated near-surface eddies located in the saltation layer, explaining the sensitivity of streamer size to wind conditions and soil particle-size distribution.

4.3. Saltation Flux Variability

[55] The interaction between saltating particles and turbulent eddies induces temporal and spatial variabilities of

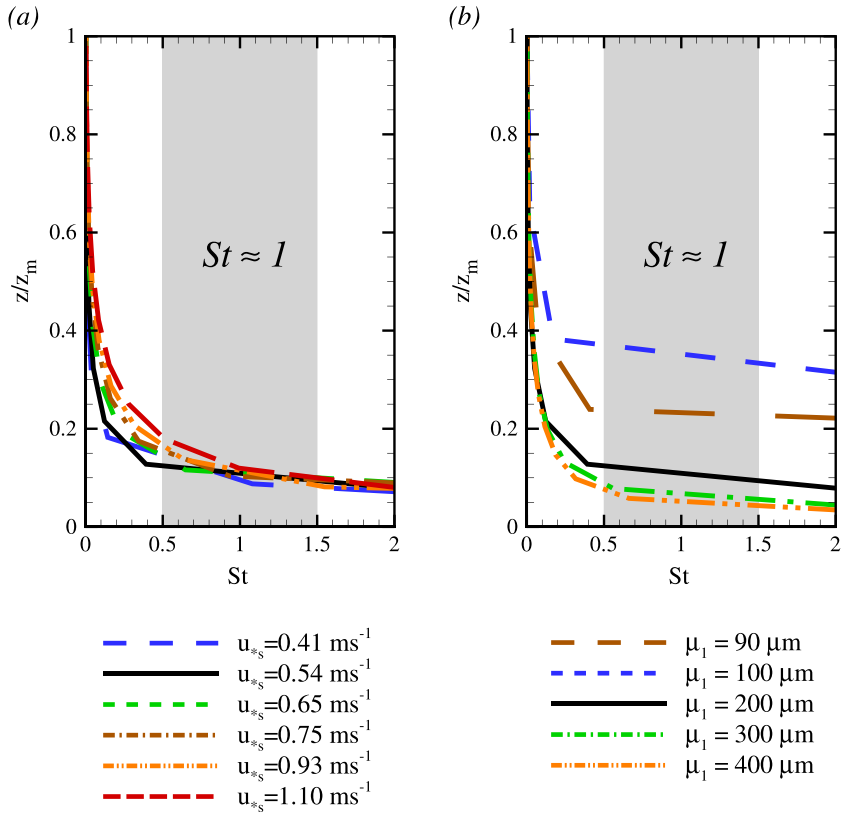

Figure 12. Mean vertical profiles of the Stoke number St for cases with (a) various saltation friction velocities u_{*s} and (b) various soil median particle diameters μ_1.

the saltation flux. The spatial variability of the saltation flux has been indirectly observed in the previous section through the sand concentration fields while the temporal variability has been observed indirectly in Figure 1 through the temporal variation of the total number of resolved particles in the computational domain. Quantifying the variability of the saltation flux due to the turbulence of flow is important in order to assess the uncertainty on flux measurement related to the flow turbulence. To that purpose, the mean standard deviation σ_G of the mean total saltation flux $\langle G_{\text{tot}} \rangle$ has been estimated from the instantaneous flux such as $\sigma_G = \sqrt{\langle G'^2_{\text{tot}} \rangle}$, and its value is presented in Figure 13 as a function of u_{*s}/u_{*t} for all simulated cases. The standard deviation of the saltation flux represents about 10% to 20% of the mean saltation flux, with a maximum for cases 4, 8, and 10. The decrease of σ_G for high u_{*s} should be related to the limited size of our computational domain as saltation processes seem to be influence by larger structures. No clear tendency of σ_G appears following the soil particle-size distribution. Unfortunately, no direct comparable values of saltation flux variability exist in the literature. Although *Gares et al.* [1996], *Jackson et al.* [2006], and *Baas and Sherman* [2006] reported saltation flux variability of about ±20% – 45% up to ±200% on sand beaches, these values (1) referred to percentages above and below the mean flux recorded from multiple trap arrays instead of standard deviations and (2) they include also variations related to surface moisture, topography, small-scale roughness elements, and sand texture, instead of only flow turbulence.

4.4. Limits of Simulations

[56] Before concluding this study, we find it important to discuss on the limits of the simulations regarding the turbulent wind flow within the saltation layer. Indeed, this region of the flow is very complex due to the large range of turbulent structure sizes involved in it and to the high concentration of saltating particles that modulates the turbulence. Evaluating the quality of the simulations in this region is difficult as measurements are

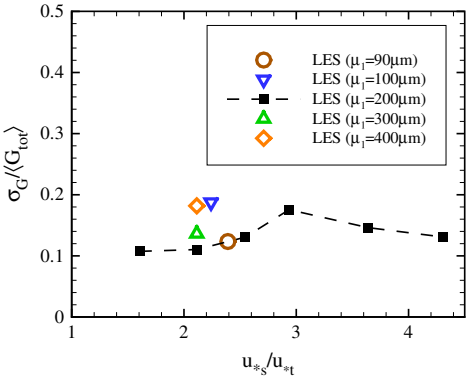

Figure 13. Standard deviation σ_G of the saltation flux normalized by the total saltation flux $\langle G_{\text{tot}} \rangle$ as a function of the saltation friction velocity u_{*s} normalized by the threshold friction velocity u_{*t}, deduced from the 10 simulated cases.

almost inexistent due to the difficulty of acquiring data in such region.

[57] The explicit simulation of turbulent eddies within the saltation layer is limited by the spatial resolution and size of our computational domain (see section 2.4). Although the characteristics of our computational domain have been chosen in order to resolve the main eddies influencing particle trajectories, still uncertainties exist (1) on the impact of subgrid-scale eddies on the resolved eddies, especially near the surface where the turbulence is mostly subgrid scale and (2) on the role of large-scale surface-layer eddies on saltation patterns when they impinge onto the surface. For the highest wind condition case as well as for the cases with smallest ($\mu_1 = 90\,\mu$m) and largest ($\mu_1 = 400\,\mu$m) particles, we probably reached the limits of our computational domain. Indeed, with small particles, small saltation patches were observed instead of elongated patterns as particles respond to smaller eddies. With large particles or high wind condition, aeolian streamers appear longer and larger, embedded in large structures that scale with the computational domain. In these cases, particles may certainly be sensitive to larger-scale eddies that could not be simulated here due to the limited size of the computational domain.

[58] The presence of high sand concentration regions in the saltation layer, as observed in simulations with high wind condition and small particles, has a strong impact on the flow as it modulates the turbulence. This turbulence modulation is still a research issue in multiphase flows, and it may be more complex than a simple turbulence reduction as considered in our model. Mechanisms of turbulence production or distortion may also occur here as in dispersed multiphase flows [*Balachandar and Eaton*, 2010]. Additionally, high sand concentration regions increase the probability of inter-particle collisions, a mechanism that was not considered in this study. Inter-particle collisions are certainly not negligible in strong saltation events and should be considered in the future version of the model. On the other hand, in low wind conditions, saltation is weaker and is very spatially intermittent as shown by the presence of individual aeolian streamer surrounded by regions of low or no sand transport. The process of particle aerodynamic entrainment from the surface is probably not negligible in low wind conditions as strong intermittent gusts reaching the surface could produce intense bursts of blowing sand.

[59] Despite these limits and the fact that turbulent structures simulated by the LES should be taken with caution close to the surface, the mean characteristics of the saltation process simulated by the present model such as the saltation roughness length and the saltation flux, are in relative good agreement with previous studies. Regarding the intermittency of saltation, for low and moderate wind conditions and for soils with median particle diameters around 200 μm, the spatial sizes of aeolian streamers are of the same order as those measured by *Baas and Sherman* [2005] from a field experiment. Furthermore, streamers become embedded in large-scale saltation patterns with increasing wind conditions as observed by *Baas and Sherman* [2005]. These results give us confidence in the ability of the present model to simulate quite accurately the interaction between turbulent eddies and saltation processes. We showed clearly that the turbulence of the flow drives the intermittency of the saltation process, meaning that saltating particles do not respond only to the mean flow. This first attempt to simulate the intermittency of the saltation appears therefore meaningful and very encouraging for simulating, in the future, saltation in more heterogeneous conditions.

5. Conclusions

[60] A new saltation model fully coupled with a Large Eddy Simulation (LES) airflow model has been developed in order to simulate and understand the complete interaction between the saltation process and the turbulent eddy structures of the flow. The model has been applied on a flat erodible soil for various wind velocity conditions and various soil particle-size distributions. The model was able to simulate a well-developed saltation layer where an average equilibrium was reached between the lower wind flow and the saltation flux. The main characteristics of the saltation layer (saltation roughness length, saltation flux, particle momentum flux) and their sensitivity to the wind conditions were qualitatively and quantitatively consistent with previous observations. We further observed that the height of the saltation layer increases with wind conditions (i.e., u_{*s}), similarly as the model prediction of *Kok and Renno* [2009] and recent wind-tunnel and field observations of *Dong et al.* [2006] and [*Dong et al.*, 2012], respectively, but weaker than the initial suggestion of *Bagnold* [1941] and *Owen* [1964] who predicted an increase proportional to u_{*s}^2 instead of u_{*s} here.

[61] The explicit simulation of the flow turbulent eddies allowed us to show the impact of such structures on the saltation process, meaning that saltating particles do not respond only to the mean flow. We observed in particular the formation of aeolian streamers in most of our simulations. To our knowledge, such structures have never been simulated before. Individual streamers were mostly visible for low to high wind conditions with $u_{*s} \leq 0.93\,\mathrm{m\,s^{-1}}$ and intermediate soil median particle diameter (around 200 μm). For very high wind conditions ($u_{*s} \geq 1\,\mathrm{m\,s^{-1}}$) and extreme saltating particle diameters (lower than 100 μm or higher than 400 μm), the resolution and size of our computation was probably not adapted to simulate streamers explicitly. Nevertheless, a remarkable similarity has been observed between the streamers simulated by our model and those identified by *Baas and Sherman* [2005] from a field experiment. The streamer sizes were of the same order of magnitude. Furthermore, we both observed that streamers become embedded in larger structures with increasing wind conditions. On the other hand, the streamer sizes (longitudinal and lateral spacing) were observed to decrease with increasing wind velocity in our simulations while *Baas and Sherman* [2005] observed no dependence between streamers size and the mean flow characteristics. In fact, this discrepancy may simply be related to the identification/definition of streamers that become more complex in high wind condition as they are embedded in large-scale saltation patterns. The streamer sizes were also observed to increase with soil particle diameters.

[62] From a correlation analysis, we confirmed previous thoughts of *Baas and Sherman* [2005] that aeolian streamers are related to elongated near-surface eddies located in the saltation layer. This link between aeolian streamers and

turbulent eddies explains the sensitivity of streamer size to wind conditions and soil particle-size distribution. Indeed, the size of turbulent eddies is influenced by the main characteristics of the saltation layer such as the saltation roughness length and the total saltation flux that change with wind condition and soil particle-size distribution. Additionally, saltation patterns are less sensitive to the lower eddies of the saltation layer with increasing wind conditions and soil particle diameters ($90 \leq \mu_1 \leq 400\,\mu$m) as the eddy lifetime decreases within the saltation layer and the particle response time increases with particle diameter. This attenuation of saltating particle sensitivity to lower eddies emphasizes the impact of large eddies on saltation patterns, accentuated by the increase of the saltation layer height. The intermittency of the saltation flux associated to these saltation patterns was estimated as 10% to 20% of the mean saltation flux.

[63] Since high sand concentration regions were correlated with high wind velocity regions, we suspect that streamers observed in our simulations are initiated by splashing process of particles carried by near-surface eddies. As elevated particles are accelerated by wind gusts, when they reach the surface, they have more energy than other particles, and so they eject more particles with more energy. Hence, streamers can be seen as the visual footprint of past turbulent eddies. The suggestion of *Baas and Sherman* [2005] that aeolian streamers form from near-surface gusts reaching the surface and initiating saltation along their path could not be verified here as the process of particle aerodynamic entrainment from the surface was not considered in the simulations.

[64] In the future, the LES model developed in this study could be used in heterogeneous configurations such as complex terrain or in presence of vegetation in order to better understand saltation process in real environment. This model could be also extended to dust particles by accounting for the ejection of dust particles resulting from sandblasting.

Appendix A: Subgrid-Scale Model

[65] The conservation equation for the SGS turbulent kinetic energy e writes:

$$\frac{\partial e}{\partial t} + \tilde{u}_j \frac{\partial e}{\partial x_j} = -\tau_{ij} \frac{\partial \tilde{u}_i}{\partial x_j} + \frac{\partial}{\partial x_j}\left(2\left((1-\delta_{j3})\nu_{th} + \delta_{j3}\nu_{tv}\right)\frac{\partial e}{\partial x_j}\right) - \frac{g}{\overline{\theta}}\tau_{3\theta} - \epsilon - \frac{Q}{V_{\text{cell}}}\sum_{p=1}^{n_{\text{pcell}}}\frac{m_p}{\overline{\rho}}\frac{2e}{T_p + T_L} f(Re_p) \quad \text{(A1)}$$

where ν_{th} and ν_{tv} are the horizontal and vertical eddy viscosities, $\tau_{3\theta}$ is the subgrid heat flux, ϵ is the dissipation rate of SGS TKE via the inertial eddy cascade, T_p ($= \rho_p d_p^2/(18\overline{\rho}\nu)$) is the particle response time, T_L ($= 4e/3C_0\epsilon$ where C_0 is the Lagrangian constant) is the Lagrangian correlation time scale. See *Dupont et al.* [2010] for further information on the parameterizations of ν_{th}, ν_{tv}, $\tau_{3\theta}$ and ϵ.

[66] The terms on the right-hand side of equation (A1) represent, respectively, the dynamic shear production term, the turbulent transport term, the buoyancy production term, the dissipation term via the inertial eddy cascade and the dissipation rate of SGS TKE through work against particle drag. The latter represents the energy-loss process that accelerates the dissipation of turbulence in the saltation layer. It is modeled similarly as in *Vinkovic et al.* [2006].

[67] **Acknowledgments.** We would like to thank the Center for Analysis and Prediction of Storms (CAPS) at the University of Oklahoma for providing the ARPS code. Computer simulations related to this work were performed using the Avakas cluster from MésoCentre MCIA as well as the EPHYSE cluster. Thanks are expressed to the EPHYSE computing team (Patrick Moreau, Tovo Rabemanantsoa, Guy Pracros, and Mark R. Irvine) for their help with the cluster set-up and administration. We would like to thank Ivana Vinkovic for providing her initial Lagrangian model and Mark R. Irvine for his help with the parallelization of the Lagrangian model inside ARPS. Financial support from the program "PEDO COTESOF" of the Agence Nationale de la Recherche (ANR) is gratefully acknowledged. Finally, we thank A.C.W. Baas, J.F. Kok, and one anonymous reviewer for their helpful comments.

References

Adrian, R. J., C. D. Meinhart, and C. D. Tomkins (2000), Vortex organization in the outer region of the turbulent boundary layer, *J. Fluid Mech.*, *422*, 1–54.

Almeida, M. P., J. S. Andrade, and H. J. Herrmann (2006), Aeolian transport layer, *Phys. Rev. Lett.*, *96*, 018001.

Almeida, M. P., J. S. Andrade, and H. J. Herrmann (2007), Aeolian transport of sand, *Eur. Phys. J. E*, *22*, 195–200.

Anderson, R. S. (1989), Saltation of sand: A qualitative review with bilogical analogy, *Proc. R. Soc. Edinburgh*, *96B*, 149–1 65.

Anderson, R. S., and P. K. Haff (1988), Simulation of eolian saltation, *Science*, *241*(4867), 820–823.

Anderson, R. S., and P. K. Haff (1991), Wind modification and bed response during saltation of sand in air, *Acta Mech.*, *1*, 21–51.

Andreotti, B. (2004), A two-species model of aeolian sand transport, *J. Fluid Mech.*, *510*, 47–70.

Baas, A. C. W. (2008), Challenges in aeolian geomorphology: Investigating aeolian streamers, *Geomorphology*, *93*, 3–16.

Baas, A. C. W., and D. J. Sherman (2005), Formation and behavior of aeolian streamers, *J. Geophys. Res.*, *110*, F03011, doi:10.1029/2004JF000270.

Baas, A. C. W., and D. J. Sherman (2006), Spatiotemporal variability of aeolian sand transport in a coastal dune environment, *J. Coastal Res.*, *22*, 1198–1205.

Bagnold, G. A (1937), The transport of sand by wind, *Geogr. J.*, *89*, 409–438.

Bagnold, G. A. (1941), *The Physics of Blown Sand and Desert Dunes*, 265 pp., Methuen, London.

Balachandar, S., and J. K. Eaton (2010), Turbulent dispersed multiphase flow, *Annu. Rev. Fluid Mech.*, *42*, 111–133.

Beladjine, D., M. Ammi, L. Oger, and A. Valance (2007), Collision process between an incident bead and a three-dimensional granular packing, *Phys. Rev. E*, *75*, 061305.

Bell, M. L., J. K. Levy, and Z. Lin (2008), The effect of sandstorms and air pollution on cause-specific hospital admissions in Taipei, Taiwan, *Occup. Environ. Med.*, *65*, 104–111.

Bhaganagar, K., J. Kim, and G. Coleman (2004), Effect of roughness on wall-bounded turbulence, *Flow Turbul. Combust.*, *72*, 463–492.

Bonasoni, P., P. Cristofanelli, F. Calzolari, U. Bonafé, F. Evanelisti, A. Stohl, R. van Dingenen, T. Colombo, and Y. Balkanski (2004), Aerosol-ozone correlations during dust transport episodes, *Atmos. Chem. Phys.*, *4*, 1201–1215.

Charnock, H. (1955), Wind stress on a water surface, *Q. J. R. Meteorol. Soc.*, *81*, 639–640.

Chen, P.-S., F. T. Tsai, C. K. Lin, C.-Y. Yang, C.-C. Chan, C.-Y. Young, and C.-H. Lee (2010), Ambient influenza and avian influenza virus during dust storm days and background days, *Environ. Health Perspect.*, *118*, 1211–1216.

Clift, R., J. R. Grace, and M. E. Weber (1978), *Bubbles, Drops and Particles*, 380 pp., Academic, New York.

Derbyshire, E. (2007), Natural minerogenic dust and human health, *Ambio*, *36*, 73–77.

Dong, Z., N. Huang, and X. Liu (2005), Simulation of the probability of midair interparticle collisions in an aeolian saltating cloud, *J. Geophys. Res.*, *110*, D24113, doi:10.1029/2005JD006070.

Dong, Z., G. Qian, W. Luo, and H. Wang (2006), Analysis of the mass flux profiles of an aeolian saltating cloud, *J. Geophys. Res.*, *111*, D16111, doi:10.1029/2005JD006630.

Dong, Z., P. Lv, Z. Zhang, G. Qian, and W. Luo (2012), Aeolian transport in the field: A comparison of the effects of different surface treatments, *J. Geophys. Res.*, *117*, D09210, doi:10.1029/2012JD017538.

Drobinski, P., and R. C. Foster (2003), On the origin of near-surface streaks in the neutrally stratified planetary boundary layer, *Boundary Layer Meteorol.*, *108*, 247–256.

Dupont, S., F. Gosselin, C. Py, E. de Langre, P. Hemon, and Y. Brunet (2010), Modelling waving crops using large-eddy simulation: Comparison with experiments and a linear stability analysis, *J. Fluid Mech.*, *652*, 5–44.

Durn, O., and H. J. Herrmann (2006), Modelling of saturated sand flux, *J. Stat. Mech.*, *2006*, P07011.

Durn, O., P. Claudin, and B. Andreotti (2011), On aeolian transport: Grain-scale interactions, dynamical mechanisms and scaling laws, *Aeolian Res.*, *3*, 243–270.

Farrell, E. (1999), An investigation of surface-wind systems for aeolian saltation: Field and laboratory experiments, Master's thesis, Dep. of Geogr., Univ. of South. Calif., Los Angeles.

Fesquet, C., S. Dupont, P. Drobinski, T. Dubos, and C. Barthlott (2009), Impact of terrain heterogeneity on coherent structure properties: Numerical approach, *Boundary Layer Meteorol.*, *133*, 71–92.

Field, J., J. Belnap, D. Breshears, J. Neff, G. Okin, J. Whicker, T. Painter, S. Ravi, M. Reheis, and R. Reynolds (2010), The ecology of dust, *Front. Ecol. Environ.*, *8*, 423–430.

Gares, P., R. Davidson-Arnott, B. Bauer, D. Sherman, R. Carter, D. Jackson, and K. Nordstrom (1996), Alongshore variations in aeolian sediment transport: Carrick Finn Strand, Ireland, *J. Coastal Res.*, *12*, 673–682.

Gillette, D. A., and W. Chen (1999), Size distributions of saltating grains: An important variable in the production of suspended particles, *Earth Surf. Processes Landforms*, *24*, 449–462.

Gillette, D. A., D. W. Fryrear, J. B. Xiao, P. Stockton, D. Ono, P. J. Helm, T. E. Gill, and T. Ley (1997), Large-scale variability of wind erosion mass flux rates at Owens Lake 1. Vertical profiles of horizontal mass fluxes of wind-eroded particles with diameter greater than 50 μm, *J. Geophys. Res.*, *102*(D22), 25,977–25,987.

Greeley, R., D. G. Blumberg, and S. H. Williams (1996), Field measurements of the flux and speed of wind-blown sand, *Sedimentology*, *43*, 41–52.

Hommema, S. E., and R. J. Adrian (2003), Packet structure of surface eddies in the atmospheric boundary layer, *Boundary Layer Meteorol.*, *106*(1), 147–170.

Huang, N., Y. Zhang, and R. D'Adamo (2007), A model of the trajectories and midair collision probabilities of sand particles in a steady state saltation cloud, *J. Geophys. Res.*, *112*, D08206, doi:10.1029/2006JD007480.

Iversen, J. D., and K. R. Rasmussen (1999), The effect of wind speed and bed slope on sand transport, *Sedimentology*, *46*, 723–731.

Jackson, N., D. Sherman, A. Hesp, A. Klein, F. Ballasteros Jr., and K. Nordstrom (2006), Small-scale spatial variations in aeolian sediment transport on a fine-sand beach, *J. Coastal Res.*, *39*, 379–383.

Kaimal, J. C., and J. J. Finnigan (1994), *Atmospheric Boundary Layer Flows. Their Structure and Measurements*, 289 pp., Oxford Univ. Press, New York.

Kawamura, R., (1951), Study of sand movement by wind, *Tech. Rep., HEL-2-8*, 57 pp., Hydraul. Eng. Lab., Univ. of Calif., Berkeley.

Kok, J. F., and N. O. Renno (2008), Electrostatics in wind-blown sand, *Phys. Rev. L*, *100*, 014501.

Kok, J. F., and N. O. Renno (2009), A comprehensive numerical model of steady state saltation (comsalt), *J. Geophys. Res.*, *114*, D17204, doi:10.1029/2009JD011702.

Lammel, M., D. Rings, and K. Kroy (2012), A two-species continuum model for aeolian sand transport, *New J. Phys.*, *14*, 093037.

Lettau, K., and H. Lettau (1978), Experimental and micro-meteorological field studies of dune migration, in *Exploring the World's Driest Climate, Rep. 101*, edited by H. H. Lettau and K. Lettau, pp. 110–147, Inst. for Environ. Stud., Univ. of Wisc., Madison.

Levin, Z., A. Teller, E. Ganor, and Y. Yin (2005), On the interactions of mineral dust, sea-salt particles, and clouds: A measurement and modeling study from the Mediterranean Israeli Dust Experiment campaign, *J. Geophys. Res.*, *110*, D20202, doi:10.1029/2005JD005810.

Li, X.-Y., L.-Y. Liu, and J.-H. Wang (2004), Wind tunnel simulation of aeolian sandy soil erodibility under human disturbance, *Geomorphology*, *59*, 3–11.

Marticorena, B., and G. Bergametti (1995), Modeling the atmospheric dust cycle: 1. Design of a soil-derived dust emission scheme, *J. Geophys. Res.*, *100*(D8), 16,415–16,430.

Miller, R., and I. Tegen (1998), Climate response to soil dust aerosols, *J. Clim.*, *11*, 3247–3267.

Nalpanis, P., J. C. R. Hunt, and C. F. Barrett (1993), Saltating particles over flat beds, *J. Fluid Mech.*, *251*, 661–685.

Namikas, S. L. (2003), Field measurement and numerical modelling of aeolian mass flux distributions on a sandy beach, *Sedimentology*, *50*, 303–326.

Nikuradse, J., (1933), Laws of flow in rough pipes (1950 translation), *Tech. Memo., 1292*, Natl. Advis. Comm. on Aeronaut., Washington, D. C.

Owen, P. R. (1964), Saltation of uniform grains in air, *J. Fluid Mech.*, *20*, 225–242.

Pahtz, T., J. F. Kok, and H. J. Herrmann (2012), The apparent surface roughness of a sand surface blown by wind from an analytical model of saltation, *New J. Phys.*, *14*, 043035.

Pope, S. B. (2000), *Turbulence Flows*, 806 pp., Cambridge Univ. Press, Cambridge, U. K.

Rasmussen, K. R., and M. Sorensen (2008), Vertical variation of particle speed and flux density in aeolian saltation: Measurement and modeling, *J. Geophys. Res.*, *113*, F02S12, doi:10.1029/2007JF000774.

Rasmussen, K. R., M. Sorensen, and B. B. Willetts (1985), Measurement of saltation and wind strength on beaches, in *Proceedings of International Workshop on the Physics of Blown Sand,* vol. 8(2), edited by O. E. Barndorff-Nielsen et al., pp. 301–326, Dep. of Theor. Stat., Aarhus Univ., Aarhus, Denmark.

Raupach, M. R. (1991), Saltation layers, vegetation canopies and roughness lengths, *Acta Mech. Suppl.*, *1*, 83–96.

Rice, M. A., B. B. Willetts, and I. K. McEwan (1995), An experimental study of multiple grain-size ejecta produced by collisions of saltating grains with a flat bed, *Sedimentology*, *42*, 695–706.

Rosenfeld, D., Y. Rudich, and R. Lahav (2001), Desert dust suppressing precipitation: A possible desertification feedback loop, *Proc. Natl. Acad. Sci. U. S. A.*, *98*, 5975–5980.

Schlesinger, P., Y. Mamane, and I. Grishkan (2006), Transport of microorganisms to Israel during Saharan dust events, *Aerobiologia*, *22*, 259–273.

Schulz, M., et al. (2012), Atmospheric transport and deposition of mineral dust to the ocean: Implications for research needs, *Environ. Sci. Technol.*, *46*, 10,390–10,404.

Shao, Y. (2008), *Physics and Modelling of Wind Erosion,* 2nd ed., 452 pp., Springer, Heidelberg, Germany.

Shao, Y., and A. Li (1999), Numerical modelling of saltation in the atmopsheric surface layer, *Boundary Layer Meteorol.*, *91*, 199–225.

Shao, Y., and H. Lu (2000), A simple expression for wind erosion threshold friction velocity, *J. Geophys. Res.*, *105*(D17), 22,437–22,443.

Shao, Y., and M. R. Raupach (1992), The overshoot and equilibration of saltation, *J. Geophys. Res.*, *97*(D18), 20,559–20,564.

Sherman, D. (1992), An equilibrium relationship for shear velocity and apparent roughness length in aeolian saltation, *Geomorphology*, *4*, 419–431.

Sherman, D., and E. Farrell (2008), Aerodynamic roughness lengths over movable beds: Comparison of wind tunnel and field data, *J. Geophys. Res.*, *113*, F02S08, doi:10.1029/2007JF000784.

Sokolik, I. N., D. M. Winker, G. Bergametti, D. A. Gillette, G. Carmichael, Y. J. Kaufman, L. Gomes, L. Schuetz, and J. E. Penner (2001), Introduction to special section: Outstanding problems in quantifying the radiative impacts of mineral dust, *J. Geophys. Res.*, *106*(D16), 18,015–18,027.

Sorensen, M. (1991), An analytic model of wind-blown sand transport, *Acta Mech. Suppl.*, *1*, 67–81.

Sorensen, M. (2004), On the rate of aeolian transport, *Geomorphology*, *59*, 53–62.

Sterk, G. (2003), Causes, consequences and control of wind erosion in Sahelian Africa, *Land Degrad. Dev.*, *14*, 95–108.

Stout, J. E., and T. M. Zobeck (1997), Intermittent saltation, *Sedimentology*, *44*, 959–970.

Stull, R. (1988), *An Introduction to Boundary Layer Meteorology*, 666 pp., Kluwer Acad. Pub, Dordrecht, Netherlands.

Tegen, I. (2003), Modeling the mineral dust aerosol cycle in the climate system, *Quat. Sci. Rev.*, *22*, 1821–1834.

Ungar, J. E., and P. K. Haff (1987), Steady state saltation in air, *Sedimentology*, *34*, 289–299.

Vinkovic, I., C. Aguirre, M. Ayrault, and S. Simoëns (2006), Large-eddy simulation of the dispersion of solid particles in a turbulent boundary layer, *Boundary Layer Meteorol.*, *121*, 283–311.

Wang, Q., and K. D. Squires (1996), Large eddy simulation of particle-laden turbulent channel flow, *Phys. Fluids*, *8*, 1207–1223.

Werner, B. T. (1990), A steady-state model of wind-blown sand transport, *J. Geol.*, *98*(1), 1–17.

White, B. (1979), Soil transport by winds on Mars, *J. Geophys. Res.*, *84*(B9), 4643–4651.

Xue, M., K. K. Droegemeier, V. Wong, A. Shapiro, and K. Brewster (1995), *ARPS Version 4.0 User's Guide*, 380 pp., Cent. for Anal. and Predict. of Storms, Univ. of Okla., Norman.

Xue, M., K. K. Droegemeier, and V. Wong (2000), The Advanced Regional Prediction System (ARPS) - A multi-scale nonhydrostatic atmospheric simulation and prediction model. Part I: Model dynamics and verification, *Meteorol. Atmos. Phys.*, *75*(3-4), 161–193.

Xue, M., K. K. Droegemeier, V. Wong, A. Shapiro, K. Brewster, F. Carr, D. Weber, Y. Liu, and D. Wang (2001), The Advanced Regional Prediction System (ARPS) - A multi-scale nonhydrostatic atmospheric simulation and prediction tool. Part II: Model physics and applications, *Meteorol. Atmos. Phys.*, *76*(3-4 p.), 143–165.

Yamamoto, Y., M. Potthoff, T. Tanaka, T. Kajishima, and Y. Tsuji (2001), Large-eddy simulation of turbulent gas-particle flow in a vertical channel: Effect of considering inter-particle collisions, *J. Fluid Mech.*, *442*, 303–334.

Yin, Y., S. Wurzler, Z. Levin, and T. G. Reisin (2002), Interactions of mineral dust particles and clouds: Effects on precipitation and cloud optical properties, *J. Geophys. Res.*, *107*(D23), 4724, doi:10.1029/2001JD001544.